

In vivo multi-scale clinical photoacoustic imaging for analysis of skin vasculature and pigmentation: a comparative review

Junho Ahn,^{a,†} Minseong Kim,^{a,†} Chulhong Kim,^{a,b,*} and Wonseok Choi^{c,*}

^aDepartment of Convergence IT Engineering, Electrical Engineering, Mechanical Engineering, and Medical Science and Engineering, Pohang University of Science and Technology, Pohang, Republic of Korea

^bOpticho Inc., Pohang, Republic of Korea

^cDepartment of Biomedical Engineering and Medical Sciences, College of Medicine, The Catholic University of Korea, Seoul, Republic of Korea

Abstract. Photoacoustic imaging (PAI) is a non-invasive imaging technique that combines the principles of optical and ultrasound imaging to visualize internal biological structures at high spatial resolution. The major characteristics of PAI, such as its sensitivity to optically absorptive targets (e.g., hemoglobin and melanin), centimeters-deep imaging depth, and non-invasiveness, make it particularly effective in the diagnosis of skin diseases including cancers, inflammatory diseases, and vascular abnormalities. In this review, we categorize PAI modalities according to various imaging scales, i.e., photoacoustic microscopy (PAM), photoacoustic mesoscopy (PAMes), and photoacoustic tomography (PAT), and then discuss their applications for clinical skin imaging *in vivo*. These modalities provide clinical indicators that quantitatively describe skin vasculature and pigmentation over various spatial resolutions and scanning ranges. We then comparatively discuss and provide insights on the clinical applications of each PAI modality for diagnosing or monitoring various skin diseases.

Keywords: photoacoustic microscopy; photoacoustic mesoscopy; photoacoustic tomography; skin diagnosis; vasculature; melanin.

Received Jul. 15, 2024; revised manuscript received Sep. 6, 2024; accepted Sep. 20, 2024; published online Oct. 25, 2024.

© The Authors. Published by Hangzhou Institute of Technology of Xidian University and Chinese Laser Press under a Creative Commons Attribution 4.0 International License. Distribution or reproduction of this work in whole or in part requires full attribution of the original publication, including its DOI.

[DOI: [10.3788/AI.2024.20005](https://doi.org/10.3788/AI.2024.20005)]

1. Introduction

Photoacoustic (PA) imaging (PAI) is a biomedical imaging technique that exploits the PA effect to visualize the contrasts of optical absorption among biological tissues. The PA effect refers to the instantaneous thermal expansion of optically absorptive targets when they are illuminated by a laser pulse, followed by the generation of ultrasound (US) waves^[1,2]. A PAI system detects these waves using US transducers and then uses the signals to reconstruct PA images that show the targets in the tissue^[3]. PAI provides deeper imaging depth than optical imaging because US waves scatter less than light does within biological

tissues. The major targets of biomedical PAI include hemoglobin (Hb) and melanin, using methods that exploit their high optical absorption in the visible and near-infrared (NIR) spectral ranges^[4-7]. Therefore, PAI can provide detailed images of vascular structures or melanin distribution. To expand PAI applications, PA images can be obtained using other spectral ranges, such as ultraviolet (UV) or even x-rays^[8,9]. Using multi-wavelength laser illumination, PAI can separate the mixed PA signals from various chromophores by applying spectral unmixing techniques to their unique absorption spectra^[10-12]. Spectral unmixing of oxy-hemoglobin (HbO₂) and deoxy-hemoglobin (HbR) is used to measure the hemoglobin oxygen saturation (sO₂) which serves as a biomarker for malignant tumors. Exogenous PA agents can be used to increase the spatial resolution, signal-to-noise ratio (SNR), and imaging depth, and enable target-specific drug delivery monitoring or theragnosis in

*Address all correspondence to Chulhong Kim, chulhong@postech.edu; Wonseok Choi, wonseok.choi@catholic.ac.kr

[†]These authors contributed equally to this work.

combination with photothermal therapy^[13–16]. While most of the PAI applications are based on the linearity of PA signal amplitude with respect to the optical properties, the nonlinearity of the PA signal can be utilized to achieve super-resolution imaging or functional imaging such as thermometry^[17,18]. PAI is frequently combined with US imaging^[19–22] or with other optical imaging modalities [e.g., optical coherence tomography (OCT) or fluorescence imaging]^[23,24] to provide complementary structural or functional information. Further, deep learning has been applied to PAI to improve image reconstruction performance and spatial or temporal resolutions^[25,26].

These advantages make PAI suitable for various fields of pre-clinical research such as neuroimaging, ophthalmic imaging, skin imaging, cancer imaging, and cardiovascular or peripheral vascular imaging. Neuroimaging applications of PAI provide a high-resolution mapping of sO₂ in brain vasculature and can monitor microhemorrhages, so the method is useful in pre-clinical studies of brain anomalies such as stroke^[27–31]. In ophthalmic imaging, PAI can show retinal vasculature and sO₂ and melanin in the retinal pigment epithelium; this information is useful in diagnosing ocular diseases^[24,32–35]. PAI can also be used in studies to quantify vascular changes induced by medications^[36].

In some areas, PAI is also being applied to clinical studies as well as pre-clinical research^[37–39]. In cancer imaging, PAI is effective in visualizing tumor angiogenesis and hypoxia related to the malignancy of the cancerous lesion such as thyroid cancer and breast cancer^[40–47]. In cardiovascular imaging, the ability of PAI to detect lipids has been exploited to characterize and monitor atherosclerotic plaques^[48–51]. PAI can visualize vasculature and thus help to assess peripheral vascular diseases^[21,52–55]. PAI can visualize microvascular structure and dynamics, particularly in the skin^[56].

Among these clinical applications, PAI is especially useful for diagnosing and monitoring skin diseases, such as inflammations, wounds, and skin cancer, which are accompanied by abnormal changes in the vasculature or melanin distribution^[57–59]. For example, melanoma, psoriasis, dermatitis, and port-wine stains (PWS) have distinct structures of blood vessels around lesions, and melasma and melanoma are strongly associated with abnormal melanin distribution^[60–66].

Conventional diagnostic tools for skin diseases include skin biopsies and optical or US imaging, but these methods are invasive, require subjective evaluation, or have low sensitivity. Skin biopsy for histological examination is the gold standard for diagnosing many skin diseases, but it leaves a wound and can facilitate infection; it is also impractical for assessing large lesions^[67]. Optical imaging such as photography or fluorescence imaging (i.e., Wood's lamp) can be performed *in vivo* to visually evaluate the color, size, or boundary of the lesions, but it can only assess superficial skin features to depths of <1 mm. Conversely, US imaging can image centimeters into the tissue but lacks the sensitivity to visualize pigmentation or microvascular structures effectively. Recently, the ultrafast Doppler (UFD) technique has been used for imaging highly vascular organs such as kidneys^[68], but it has not been used yet for investigating skin microvasculature. PAI is non-invasive, has a high spatial resolution, and is sensitive to Hb and melanin; therefore, the method can effectively overcome these limitations of conventional methods. PAI can visualize the microvascular structure and melanin distribution below the skin surface with high contrast and can provide quantitative evaluation of these features to enable distinction between lesions of different skin diseases.

In this review, we discuss clinical PAI techniques for imaging human skin to resolutions ranging from micrometers to millimeters. First, we introduce the principles of the PAI modalities used for skin imaging in three categories (Fig. 1) according to the scale: PA microscopy (PAM), PA mesoscopy (PAMes), and PA tomography (PAT). Next, we discuss PAI applications to image two types of imaging targets in the skin: vasculature only or vasculature plus melanin. To the best of our knowledge, there were only several recent PAI reports that discussed melanin imaging only, and thus we partially included the vascular imaging in the latter section. Each section is divided into three subsections that present uses of PAM, PAMes, and PAT, respectively, to compare their different imaging scales of the same imaging target. We review peer-reviewed papers published from 2018 to 2024, with a focus on imaging techniques for human skin, and on clinical indicators that consider vasculature and melanin. We then analyze the general relationship between spatial resolution and imaging depth or field-of-view (FOV) to guide the selection of an appropriate PAI modality for specific skin-imaging applications.

2. Clinical PAI Modalities for Skin Imaging

The major components of PAI systems are the optical excitation source (i.e., laser) and the acoustic detector (i.e., US transducer). Both the optical beam delivery and acoustic detection can be made either focused or unfocused (or diffuse), depending on the desired imaging depth and spatial resolution. In biological tissues, scattering is more than US waves, so each photon can ballistically travel up to only ~1 mm on average (i.e., transport mean free path). Therefore, the optical beam can only be focused at <1 mm depth in biological tissues; beyond that depth, the beam diffuses randomly. Contrarily, the generated US waves scatter much less and can be focused at depths from several millimeters to centimeters, but attenuation of the waves tends to increase as their frequency increases. Therefore, depending on the system configuration, PAI can provide either high spatial resolution at a shallow depth or low spatial resolution at a deep depth. Generally, PAI is categorized into three modalities: PAM, which uses a focused laser and a focused US detector to achieve the finest spatial resolution at shallow depths; PAMes, which uses an unfocused laser and a high-frequency focused US to achieve high resolution and less superficial imaging depth; and PAT, which uses an unfocused (diffused) laser and multiple low-frequency unfocused US transducers (i.e., a US transducer array) to achieve deep imaging depth but low spatial resolution.

A typical PAM system consists of a single-element focused US transducer, a laser source (usually emitting $\lambda = 532$ nm) with its focusing optics, and an optical-acoustic beam-coupling module. PAM can be further divided into two types: optical resolution PAM (OR-PAM) and acoustic resolution PAM (AR-PAM).

OR-PAM uses a tightly focused laser beam to achieve high lateral resolution typically in the range of a few micrometers. Recent improvements in OR-PAM can achieve sub-micrometer resolution using a transparent US transducer to increase the numerical aperture (NA) of the optical configuration^[9]. However, beyond the depth limit (~1 mm) of optical diffusion in biological tissues, optical scattering greatly reduces the focusing effectiveness, so lateral resolution degrades. AR-PAM can image to depths of several millimeters, so it is suitable for imaging relatively deep tissues while maintaining adequate resolution^[69].

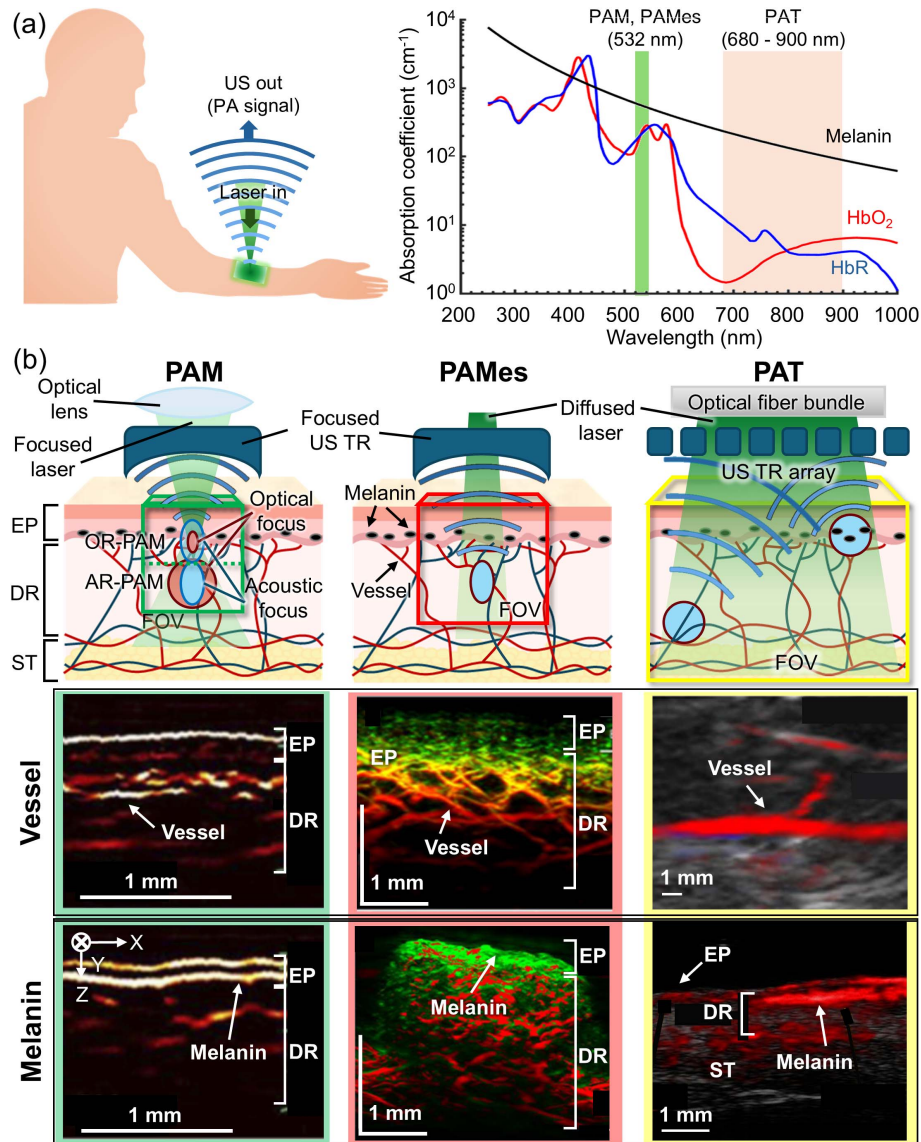


Fig. 1 PAI modalities in skin imaging. (a) A schematic of the PAI principle (left) and the optical absorption spectra of HbO₂, HbR, and melanin (right). The spectra data are from <http://omlc.orgi.edu>. (b) Conceptual schematics and example images of the vessel and melanin in the skin for each PAI modality. US, ultrasound; PA, photoacoustic; PAI, photoacoustic imaging; PAM, photoacoustic microscopy; PAMes, photoacoustic mesoscopy; PAT, photoacoustic tomography; HbR, deoxy-hemoglobin; HbO₂, oxy-hemoglobin; TR, transducer; EP, epidermis; DR, dermis; ST, subcutaneous tissue; FOV, field of view. The figures were reproduced with permission from Refs. [100] (Copyright © 2021 Optical Society of America), [120] (Copyright © 2021 Optical Society of America), [112] (Copyright © 2022 by the authors. Licensee MDPI, Basel, Switzerland), and [122] (Copyright © by the authors).

AR-PAM relies on acoustic focusing by the US transducer to achieve lateral resolution typically in tens of micrometers, which is determined by the US frequency of the transducer, NA, and the corresponding focal spot size. In principle, AR-PAM and PAMes both use a diffuse laser in relatively deep depths, but AR-PAM may use a quasi-focused laser when switchably combined with OR-PAM. In such a switchable OR/AR-PAM configuration, the acoustic focus position can be shifted to either <1 mm depth for OR-PAM or >1 mm for AR-PAM, while sharing the same laser focusing at <1 mm depth.

Both OR- and AR-PAM acquire time-resolved amplitude data (i.e., A-line data) for a single point per laser pulse. The axial resolution depends on the US frequency of the transducer. To obtain 2D or 3D images, multiple A-lines must be acquired by raster scanning using mechanical stages. PAM images are formed directly from the data acquired at the focal depth without additional reconstruction algorithms, but AR-PAM may use synthetic-aperture focusing techniques to improve lateral resolution at out-of-focus depths^[70]. Moreover, image post-processing techniques such as motion correction or vascular

signal enhancement techniques can be applied to additionally improve the PAM images^[71,72]. Further, deep-learning algorithms can be used on PAM images for automatic microvessel segmentation or virtual staining^[73,74].

However, conventional mechanical raster scanning is time-consuming and susceptible to motion artifacts, so it has limited clinical applications. Scanning speed can be increased using advanced optical or acoustic scanning systems such as Galvo scanners, micro-electromechanical system (MEMS) scanners, or polygonal mirrors^[75–79]. Laser scanning OR-PAM systems have been also proposed to increase imaging speed^[80,81]. Instead of increasing scan speeds, some studies use deep learning to increase temporal resolution by achieving sufficient resolution while requiring less data than conventional methods^[82]. Alternatively, the spatial light modulation technique enables high frame rate PAM imaging without mechanical scanning^[83].

PAMes operates on a scale between AR-PAM and PAT, typically using wide-field diffuse laser illumination and a single-element focused US transducer. PAM is similar to AR-PAM in that it is an acoustic-resolution modality using a focused US transducer. However, AR-PAM is often configured with an optical lens to focus the laser to be switchable with OR-PAM. On the contrary, PAMes uses a diffused laser to deliver higher laser power to image deeper into the tissue. PAMes stacks multiple A-lines to create 2D or 3D images, but it also uses reconstruction algorithms to increase spatial resolution and SNR^[84]. The method usually achieves imaging depths of up to 10 mm with spatial resolutions in tens of micrometers. Particularly, raster-scan optoacoustic mesoscopy (RSOM) from iThera Medical GmbH, the most widely used PAMes system, uses ultra-broadband (~100 MHz) and a high-frequency (tens of megahertz) US transducer, and divides the PA signals into two acoustic frequency bands to render small and large vessels separately^[85]. This feature provides higher axial resolution than typical PAM systems and thus provides the ability to distinguish the epidermis from the dermis within the skin tissue.

PAT targets the visualization of tissue structures within several centimeters in all directions. It uses wide-field laser illumination and a US transducer array (typically 64 to 256 elements) for tomographic image reconstruction and, therefore, can acquire a cross-sectional image (i.e., B-mode) with a single laser pulse^[86]. For 3D imaging, PAT can either use a 1D transducer array (e.g., linear and curved) with a motorized scanner or a 2D transducer array that acquires volume data at once^[87–89]. In addition, 3D handheld PAT systems have been developed for versatile imaging of healthy or diseased tissues positioned in narrow locations where conventional 3D PAI systems cannot fit in due to size^[90,91].

PAT usually uses a low-frequency (several megahertz) US array transducer, which facilitates visualization of deeper tissues than PAM or PAMes at the cost of a loss of spatial resolution (to hundreds of micrometers). Furthermore, most US transducer arrays have a limited signal reception aperture and may not fully acquire the PA waves that propagate omni-directionally, so limited-view artifacts may develop. Therefore, advancements in image reconstruction are needed to maximize the achievable image quality even in the limited signal reception environment^[92]. Recent studies have used deep learning to solve the low spatial resolution or limited-view artifacts of PAT systems^[93,94].

PAT uses a wide-field laser and, therefore, does not rely on optical focusing and does not require a very high-PRF laser, as PAM does. Therefore, multiple optical wavelengths can be used

relatively easily to estimate the relative concentrations of chromophores (e.g., HbO₂, Hb, and melanin); this method is often called multi-spectral optoacoustic tomography (MSOT).

We now compare the three PAI modalities described above (Fig. 1). The basic principle of PAI is that the laser is illuminated on the target tissue and the corresponding PA signal is generated according to the optical absorption coefficients of chromophores [Fig. 1(a)]. Typically, PAM and PAMes use the visible range to achieve high spatial resolution and sensitivity, whereas PAT can also use NIR when deep penetration is required. Many pulsed laser sources that use an optical parametric oscillator (OPO) support fast wavelength switching in the NIR range; this ability is suitable for multi-wavelength PAT or even some PAMes implementations.

The systems that use each modality have different constructions and applications, and they provide different types of images [Fig. 1(b)]. PAM and PAMes systems commonly use a focused US transducer with motorized raster scanners to acquire images, whereas PAT systems use unfocused US transducer arrays. In PAM, particularly for OR-PAM, the laser is focused at the epidermal depth (<1 mm) to achieve high lateral resolution, whereas PAMes and PAT systems use diffuse lasers. The high spatial resolution of PAM allows precise separation of each skin layer up to the superficial dermal layer and enables detailed delineation of the vasculature and melanin. PAMes can identify and analyze the structures up to deep dermal layers with a slightly degraded spatial resolution. PAT can image at a depth much deeper than the subcutaneous tissue and has a wider FOV than the other two modalities. It can show larger vessels at greater depths than the other modalities and can depict the melanin in a whole lesion across multiple layers of the skin.

3. Clinical PAI in Skin Vasculature Imaging

3.1. Clinical PAM Techniques for Imaging Skin Vasculature

Cheng *et al.* developed a typical OR-PAM system that can achieve centimeter-scale scan range (up to 40 mm × 40 mm) to image human skin microvasculature^[95]. The optical and acoustic beams are coaxially aligned by passing a 532 nm laser beam through a 3 mm central hole on a US transducer (center frequency: 40 MHz, bandwidth: 110%). The system yielded spatial resolutions of 31.2 μm axially and 5 μm laterally. One B-scan image in the 5 mm range can be acquired in about 0.1 s (step size: 5 μm, PRF: 10 kHz). To demonstrate human skin imaging, the back and palm of the hand areas of a healthy volunteer were imaged and qualitatively compared in terms of the number, depth, and diameter of dermal vasculature. The maximum PA signal detection depth was greater in the palm of the hand (~2 mm) than in the back of the hand (~1.5 mm) due to the higher concentration of melanin pigment in the back of the hand than in the palm. The distribution of vessel depths and diameters was more diverse in the palm than in the back of the hand; the difference was more obvious when using depth-encoded PA MAP images than when using regular PA MAP images.

Ahn *et al.* have combined OR-PAM and photoplethysmography (PPG) to track the movement of single blood microvessels and PPG signals simultaneously in a finger [Fig. 2(a)]^[96]. This implementation of OR-PAM used a galvanometer scanner, a flat ring-shaped US transducer, and a parabolic mirror. The galvanometer scanner allows fast B-mode scanning at a frame rate of

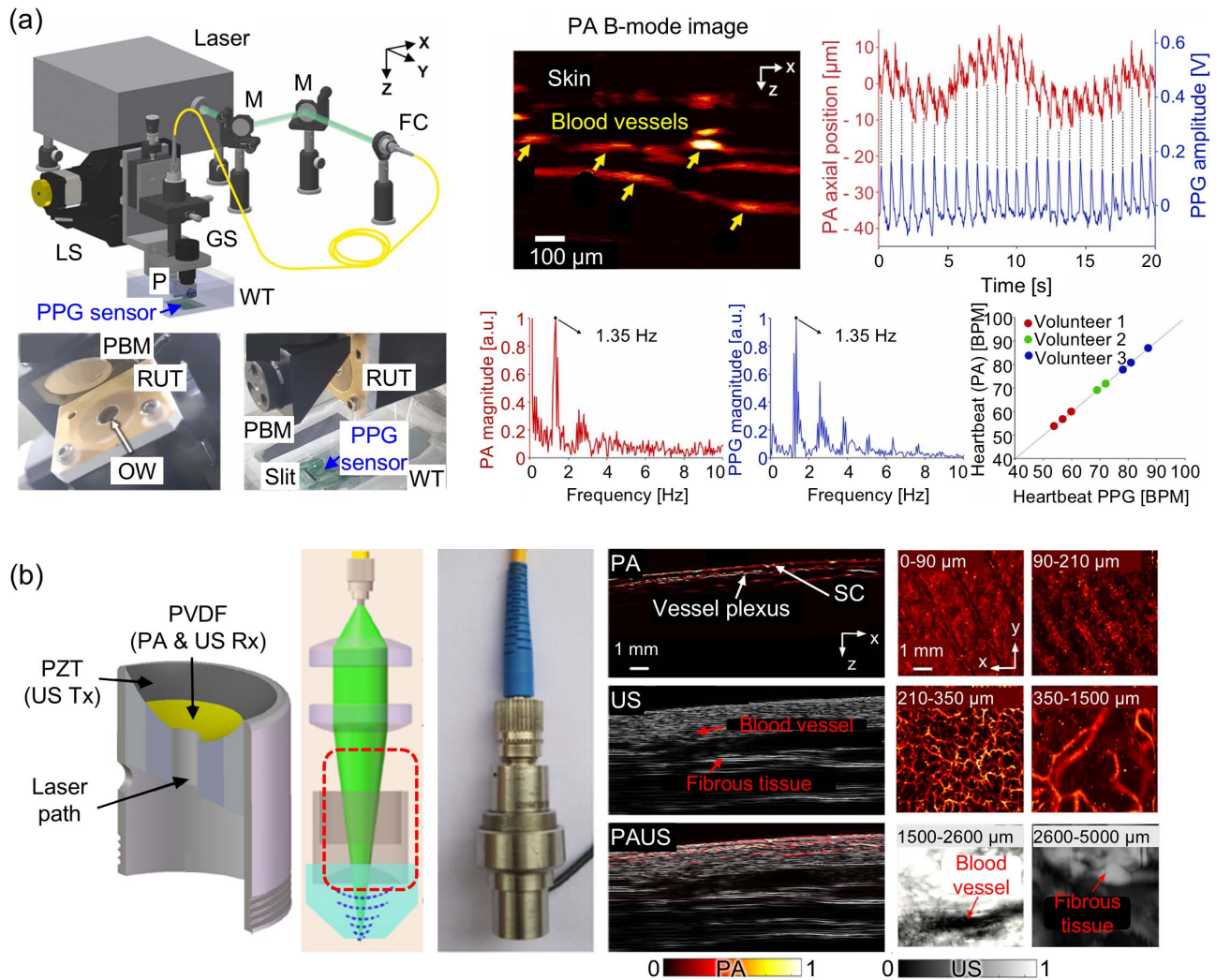


Fig. 2 PAM techniques for improved visualization of skin structures. (a) An OR-PAM system integrated with a photoplethysmography (PPG) sensor. Simultaneous real-time monitoring of PA and PPG signals from superficial dermal vessels in fingers accurately estimated the heartbeat rate (~ 1.35 Hz) of healthy volunteers. (b) Imaging probe configuration and example images of a healthy volunteer's palm skin using the dual-modal PA/US dermoscope. The transducer consisted of a PVDF transducer for PA/US signal reception and a PZT transducer for US signal transmission. PA and US images were able to depict shallow microvasculature and deeper skin structures in the palm, respectively. M, mirror; FC, fiber coupler/collimator; P, prism; GS, galvanometer scanner; WT, water tank; LS, linear stage; RUT, ring-shaped US transducer; OW, optical window; PBM, parabolic mirror; PVDF, polyvinylidene fluoride; PZT, lead zirconate titanate; PA, photoacoustic; US, ultrasound; SC, stratum corneum. The figures were reproduced with permission from Refs. [96] (Copyright © 2022 by the authors. Published by Elsevier GmbH) and [97] (Copyright © 2020 WILEY-VCH Verlag GmbH & Co. KGaA, Weinheim).

50 Hz, and the parabolic mirror steers both light and acoustic waves simultaneously with a short focal length and 2.5 μm lateral resolution. This system could simultaneously acquire cross-sectional vascular images and measure the blood volume of the finger, which were synchronous to the co-acquired PPG signals. The heart rates of three volunteers were measured using both OR-PAM and PPG, and the measurements by the two modalities agreed well.

Wang *et al.* have constructed a dual-modal PA/US dermoscope using a bimorph US transducer that uses lead zirconate titanate (PZT) (for US transmission) and polyvinylidene

fluoride (PVDF) (for PA and US reception) [Fig. 2(b)]^[97]. PZT provided strong US wave generation, and the PVDF had wide signal reception bandwidth to provide high spatial resolution. The system achieved an axial resolution of 57.8 μm for both modalities, with a lateral resolution of 45 μm for US microscopy and 6.8 μm for PAM. A human palm could be imaged to a depth of ~ 1.5 mm, which allowed high-resolution images of the stratum corneum (SC) and superficial vessel plexus, but the signal from the dermal layer was not strong enough to analyze the structure. Complementarily, US images could visualize skin up to a depth of 5 mm, where fibrous connective tissue

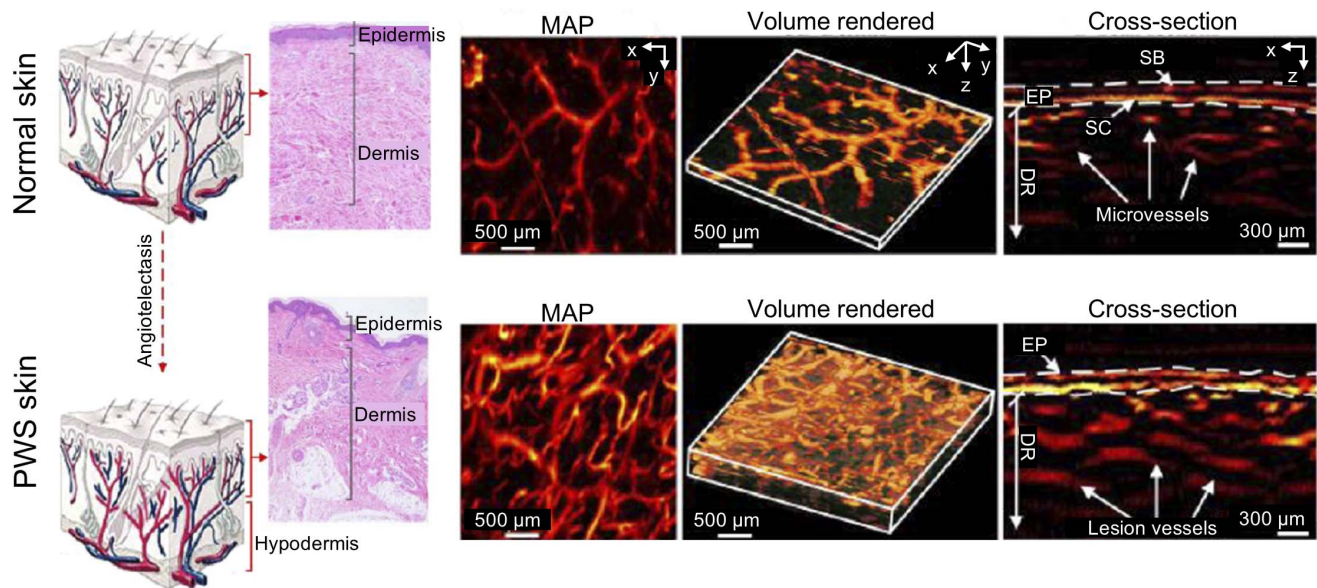


Fig. 3 Photoacoustic microscopic biopsy (PAMB) technique for port wine stain (PWS) lesion imaging. Compared to normal skins, PWS skins have dilated vascular structure in the dermal layer. MAP, maximum amplitude projection; EP, epidermis; DR, dermis; SB, stratum basale; SC, stratum corneum. The figures were reproduced with permission from Ref. [100] (Copyright © 2021 Optical Society of America).

and large blood vessels are located. This work demonstrated that the dual-modal PA/US skin imaging could fully depict the skin tissue structure as well as the microvasculature.

To increase the visibility and quantitative accuracy of PA dermoscopic images, a 4D spectral-spatial computational model of the skin has been developed^[98]. It considers the heterogeneous optical and acoustic tissue parameters. The model was built with a Monte-Carlo simulation of optical propagation, k-Wave MATLAB toolbox for acoustic simulation, and detailed modeling of the multilayered skin structure in the 3D spatial domain as well as the spectral domain (i.e., optical wavelength). A computational skin model was used to generate *in silico* PA dermoscopy data pairs (low center frequency vs. high center frequency and strong vs. weak scattering) to train two U-Net neural networks to increase the spatial resolution and imaging depth. The trained network significantly increased the axial resolution and visibility of deep vessels in images of human palm skin.

Cheng *et al.* used an extended depth-of-field PAM (E-DOF-PAM) to monitor the revascularization process during the healing of a skin wound^[99]. An elongated focus lens was added to a conventional Gaussian beam PAM (GB-PAM) system to create Bessel beams that allowed relatively uniform spatial resolution at different depths. Compared to GB-PAM, the lateral resolution of the E-DOF-PAM was slightly degraded from 4.7 to 6.5 μm , but the depth-of-field was significantly increased to nearly 1 mm. Wounded skin on a volunteer was imaged using E-DOF-PAM, and the image separately displayed the SC, stratum basale (SB), and dermal vascular layer. PAM images of the wound showed increased thickness and PA amplitude in the SC layer, disappearance of signals in the SB layer, and development of small and dense microvasculature in the dermal layer.

Ma *et al.* developed a non-invasive photoacoustic microscopic biopsy (PAMB) system to visualize and quantify dermal angiopathy with high spatial resolution and penetration

depth^[100]. The PAMB system integrates a 532 nm laser and a broadband (5–90 MHz) US transducer, and achieves axial resolutions from 34 to 57 μm and lateral resolutions from 1.5 to 104 μm (1.5 to 3.8 μm on the zero plane, 10 to 40 μm at 0.2 to 1.5 mm depth, and 40 to 140 μm at 1.5 to 3.0 mm depth in skin tissue), with a maximum imaging depth of 3 mm. This system uses an adjustable confocal opto-sono objective that allows switching among different NAs to optimize focus at various depths. The system quantified vascular parameters, including capillary-loop depth, diameter, and vascular volume, and it could distinguish healthy skin from PWS-affected skin (Fig. 3). PAMB demonstrated significant differences in vascular features among different PWS stages and, thereby, provided a quantitative assessment of lesion severity. The authors introduced a comprehensive parameter (PAFIND) that combines microvessel density and depth to enable objective evaluation of PWS severity and treatment efficacy. The study highlighted PAMB's potential for non-invasive, label-free biopsies, and it may be a valuable tool for diagnosing and monitoring skin diseases and treatment responses.

3.2. Clinical PAMes Techniques for Imaging Skin Vasculature

Hindelang *et al.* used RSOM to differentiate between allergic and irritant skin reactions in patch testing^[101]. The RSOM images were analyzed to provide quantified vascular biomarkers such as blood volume, vessel fragmentation, and frequency-content ratio. Allergic reactions showed higher vessel fragmentation and lower frequency ratios than did irritant reactions. The RSOM system used in this study consisted of a 532 nm laser and a 55 MHz US transducer. The US transducer has an ultra-broadband bandwidth of 10 to 120 MHz, so the RSOM provided images that had spatial resolutions of 8 μm axially and 30 μm

laterally, and an imaging depth of 1.5 mm. The researchers divided the detected PA signal into two frequency bands, i.e., 10 to 40 MHz to distinguish large vasculature, and 40 to 120 MHz to distinguish small vasculature [Fig. 4(a)]. Compared to dynamic optical coherence tomography (D-OCT), RSOM provided similar image quality in en face images but better quality in transverse cross-sectional images due to its axial resolution and penetration depth.

The RSOM technique has also been used to quantify skin sensitivity to UV radiation in healthy volunteers^[102]. Skin areas were exposed to increasing doses of UV radiation, and the dermal microvasculature was monitored in RSOM images. UV radiation induced vasodilation and recruitment of vessels, and the vessel fraction increased linearly with UV doses. These results suggest that RSOM can monitor and quantify UV-induced erythema with high precision.

Nau *et al.* used RSOM to measure biomarkers such as the mean capillary loop length and mean plexus width to assess the severity of atopic dermatitis (AD)^[103]. Yew *et al.* also used the method to investigate skin structure and vasculature changes in AD lesions during treatment^[104].

Li *et al.* used multispectral raster scanning optoacoustic mesoscopy (ms-RSOM) with four distinct wavelengths (532, 555, 579, and 606 nm) to obtain functional information of AD lesions^[105]. sO_2 and epidermis thickness decreased in AD lesions after treatment. The same strategy has been used to monitor psoriasis and showed that the structural indicators (epidermal thickness and total blood volume) and functional indicators (sO_2) after treatment were decreased in a psoriasis lesion^[106].

Vascular indicators in the skin provided from RSOM images have also been used to assess diabetes-related changes in dermal

microvasculature [Fig. 4(b)]^[107]. RSOM images of diabetes patients were compared to those of healthy volunteers; they were segmented and compared to derive six label-free PA biomarkers: epidermal thickness, signal density of epidermis layer, dermal blood volume, vessel diameter, small vessel number, and large vessel number. Microvascular parameters differed between diabetic patients and healthy people, with the difference being most significant in the number of vessels $<40 \mu\text{m}$ in diameter.

However, the RSOM technique has the disadvantage of a long scan time. To solve this problem, He *et al.* developed a fast RSOM (FRSOM); it significantly reduces scanning time and, thereby, minimizes motion artifacts^[108]. The FRSOM system consists of a coaxial optical-acoustic probe that uses a 532 nm laser and a 50 MHz spherically focused ring transducer with an integrated pre-amplifier to increase the SNR. Thus, FRSOM could obtain the same image quality as conventional RSOM with lower laser-pulse energy; this trait allowed an increased laser repetition rate without exceeding the laser safety limit, so scanning can be accelerated. To scan a $4 \text{ mm} \times 2 \text{ mm}$ area, the FRSOM took $<15 \text{ s}$, whereas the conventional RSOM system took 70 s. FRSOM can further minimize motion artifacts by scanning while the subject holds a single breath, so imaging of microvessel structures could be improved. FRSOM was used to visualize and quantify changes in the vessel diameter, blood volume, and vessel density during post-occlusive reactive hyperemia (RH) tests, and it detected significant differences in the maximum volume change, hyperemia ratio, and time to peak; these differences were used to quantify microvascular endothelial dysfunction in smokers and cardiovascular disease patients, compared to healthy individuals.

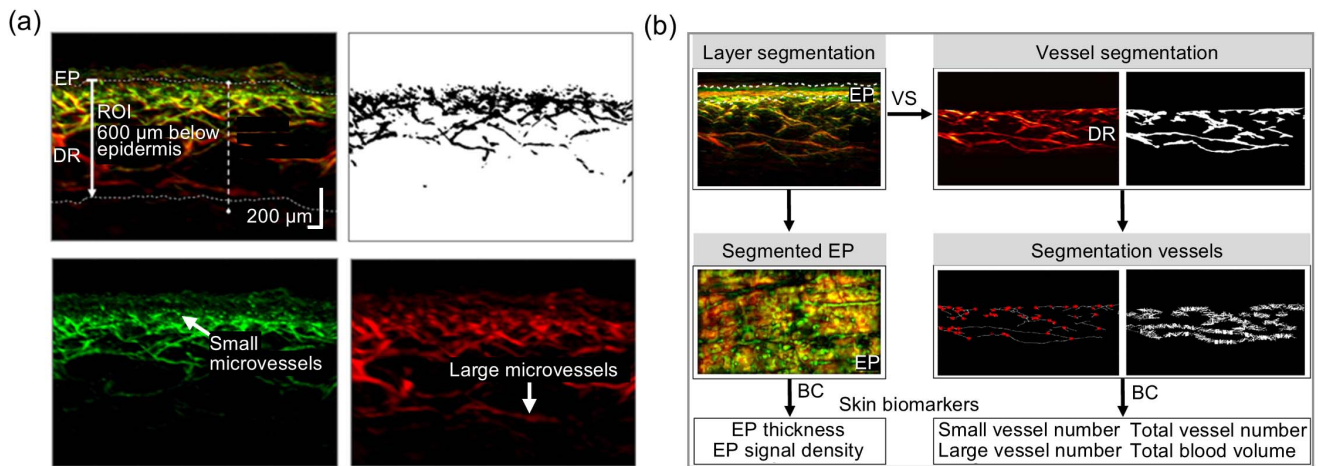


Fig. 4 (a) Cross-sectional RSOM image composed of two bandwidth signal images and a binary image of the high-frequency signal within ROI. The combined image of high-frequency signal (green, representing small vessels) and low-frequency signal (red, representing large vessels) shows the boundary between epidermis and dermis. The binary image is used to calculate the vessel fragmentation value. (b) The process of skin biomarker quantification in cross-sectional RSOM images. First, the EP and DR regions are divided, and the EP thickness and the EP signal density are calculated. Then, the vessel numbers are calculated by counting the vessel branches (red dots) in the DR area, and the total blood volume is calculated from the binary image. RSOM, raster scan optoacoustic mesoscopy; ROI, region of interest; EP, epidermis; DR, dermis; VS, vessel segmentation; BC, biomarker computation. The figures were reproduced with permission from Refs. [101] (Copyright © 2020 by the authors. Contact Dermatitis published by John Wiley & Sons Ltd.) and [107] [Copyright © 2023 by the author(s)].

3.3. Clinical PAT Techniques for Imaging Skin Vasculature

Systemic sclerosis (SSc) is an immune-mediated disease that involves fibrosis and vasculopathy of the skin and internal organs. SSc has a higher mortality rate than any other rheumatic disease^[109]. PAI has been evaluated as a method to detect changes in skin microvessels to enable early detection and quantitative assessment of these conditions. Masthoff *et al.* used MSOT Acuity Echo (iThera Medical, Munich) to analyze fingers that were afflicted with SSc^[110]. Each cross-sectional image was 30 mm × 30 mm, and the PA spatial resolution was ~190 μm. Laser pulse repetition rates for single and multispectral imaging were 25 and 5 Hz, respectively, and each examination took about 10 min. For multispectral imaging, five wavelengths 700 ≤ λ ≤ 850 nm were used to calculate HbO₂, HbR, and total hemoglobin (HbT). SSc patients showed a significant decrease in HbO₂ and HbT compared to healthy volunteers [Fig. 5(a)]. Additionally, the progressive SSc patients had lower HbR than healthy volunteers and stable SSc patients [Fig. 5(b)].

RH is a non-invasive method to assess peripheral microvasculature, which, in the simplest form, represents the magnitude of limb reperfusion following a brief period of ischemia induced by arterial occlusion^[111]. Using MSOT imaging, Rodrigues *et al.* showed that PAI can be used to observe and quantify RH *in vivo*^[112]. Superficial and deep vascular plexuses were measured at baseline, during occlusion, and after occlusion, and the corresponding HbR, HbO₂, HbT, and sO₂ were obtained from the MSOT image. Observations revealed that the occlusion collapsed the smaller superficial plexus while inducing stasis at the deeper plexus [Figs. 5(c1) and 5(c2)].

Zhang *et al.* used a PAI system that uses LEDs (AcousticX, CYBERDYNE, Inc., Tsukuba, Japan) to analyze the severity and treatment response of PWS^[113]. The system consists of a US transducer array with 128 elements and 9 MHz center frequency, and two LED arrays that had 400 μJ pulse energy, one attached on each side of the US transducer. The system provided mean axial resolution of 220 μm and mean lateral resolution of 460 μm, with an imaging depth of up to 28 mm. PWS lesions were imaged during treatment using hematoporphyrin

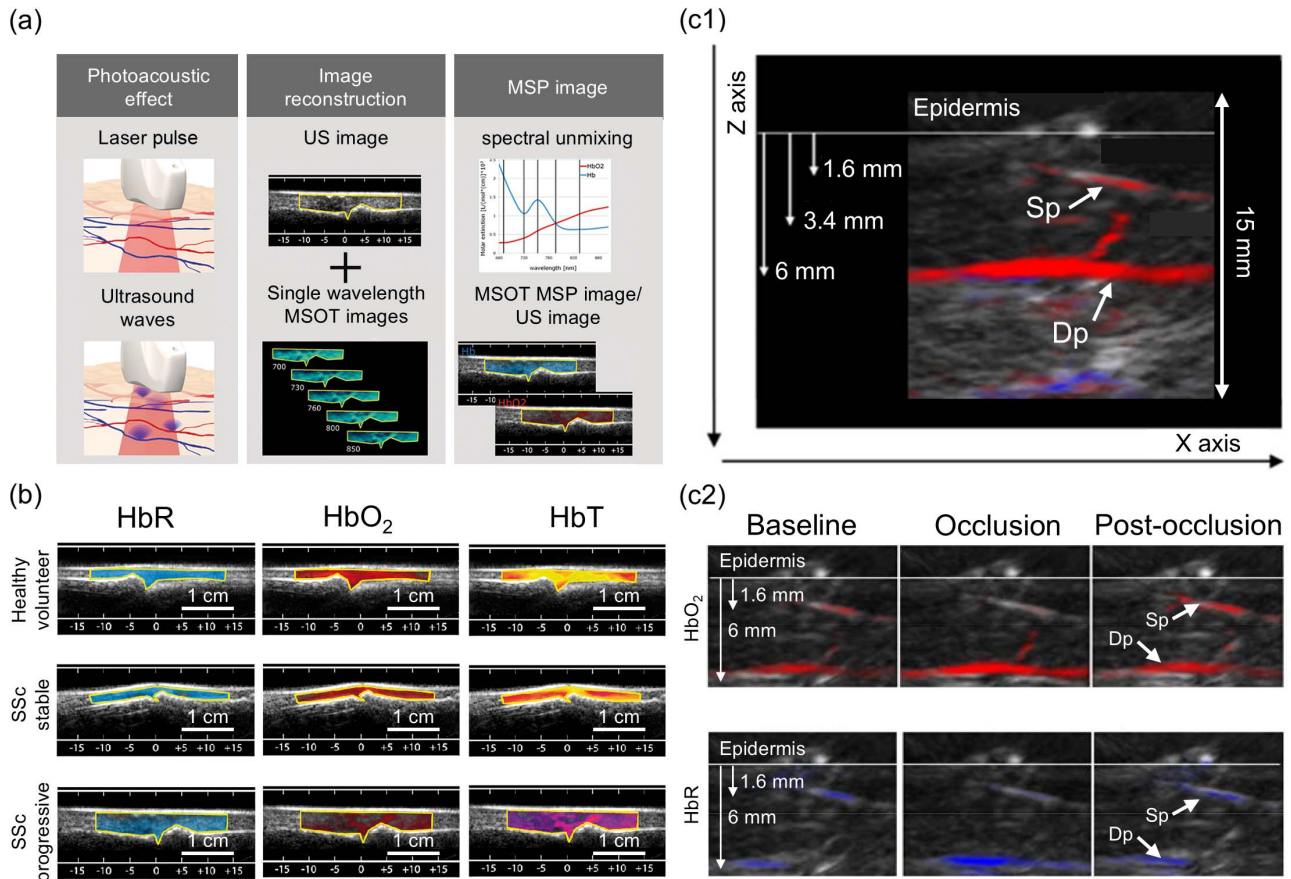


Fig. 5 PAT techniques for clinical skin vasculature imaging. (a) MSOT principle and image processing step. (b) MSOT images of HbR, HbO₂, and HbT for healthy volunteer, and patients with stable SSc and progressive SSc. (c1) MSOT images of Sp and Dp. (c2) MSOT images of HbO₂ and HbR during the reactive hyperemia. PAT, photoacoustic tomography; US, ultrasound; MSOT, multi-spectral optoacoustic tomography; MSP, multispectral pulsed; HbR, deoxy-hemoglobin; HbO₂, oxy-hemoglobin; HbT, total hemoglobin; SSc, systemic sclerosis; Sp, superficial plexus; Dp, deep plexus. The figures were reproduced with permission from Refs. [109] (Copyright © 2018 WILEY-VCH Verlag GmbH & Co. KGaA, Weinheim) and [112] (Copyright © 2022 by the authors; Licensee MDPI, Basel, Switzerland).

monomethyl ether photodynamic therapy. After treatment, PWS levels estimated from the PA signal intensity showed significant decrease.

4. Clinical PAI in Skin Vasculature and Pigmentation Imaging

4.1. Clinical PAM Techniques for Imaging Skin Vasculature and Pigmentation

Ma *et al.* reported a switchable OR-AR PAM system to image the melanin and vasculature in different skin layers of human skin [Fig. 6(a)]^[114]. A customized adjustable opto-sono objective lens was used to adjust the focal position in the axial direction, and it enabled switching between OR and AR modes. For instance, OR imaging was used when the opto-sono objective lens was positioned with its optical focus of <1 mm deep in the skin,

whereas AR imaging was used when acoustic focus was at deeper than 1 mm, where optical beams diverge. Thus, the system can visualize the different layers of human skin with high resolution at all depths, with OR-PAM used in the epidermis (0–180 μm depth) and epidermal–dermal junction (220–550 μm depth) layers, and AR-PAM used beneath the junction layer. Using the system, the melanin concentration in the SB and the vascular density below the epidermal–dermal junction were compared in the back and palm of the hand. Significantly, more melanin was detected on the back of the hand than on the palm, whereas more vessels were observed in the palm than on the back.

Instead of scanning with a fixed focal depth, an autofocusing opto-sono probe has been developed for dynamic confocusing along the skin contour [Figs. 6(b1)–6(b3)]^[115]. The main working component of the autofocusing probe was a liquid lens that exploits electrowetting; it consists of 22% NaCl solution as the

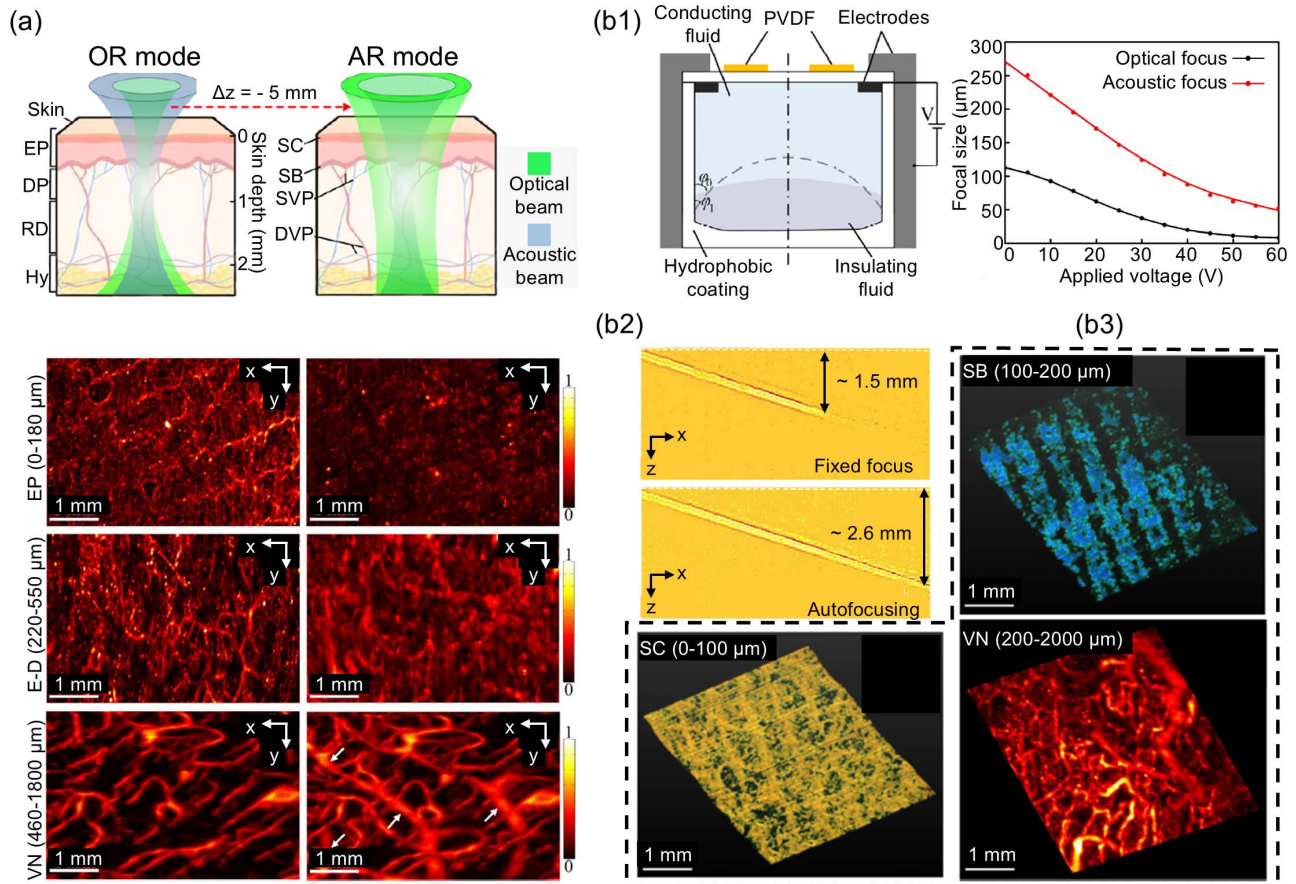


Fig. 6 Switchable OR-AR PAM techniques for skin vasculature and pigment imaging. (a) Switchable OR-AR PAM technique that alters the focusing mode by axially translating the depth of the fixed focus. (b1)–(b3) Autofocusing PAM technique using a voltage-controlled liquid lens. (b1) The focal sizes of the optical and acoustic beams were controlled by the input voltage at the electrodes. (b2) Phantom imaging demonstrated that autofocusing improved the imaging depth compared to the fixed focus mode. (b3) A healthy volunteer’s palm skin was imaged in different layers, where SC/SB layers and Va layers contained the melanin and vasculature, respectively. OR, optical resolution; AR, acoustic resolution; EP, epidermis; DP, dermal papillae; RD, reticular dermis; Hy, hypodermis; SC, stratum corneum; SB, stratum basale; SVP, superficial vascular plexus; DVP, deep vascular plexus; E-D, epidermis-dermis junction; VN, vascular network; PVDF, polyvinylidene fluoride. The figures were reproduced with permission from Refs. [114] [Copyright © 2020 by the author(s)] and [115] (Copyright © 2022 Wiley-VCH GmbH).

conducting liquid and a mixture of glycerol and silicone oil as the insulating liquid. When electrical voltage was applied between the adjacent electrodes, the curvature radius of the interface between the two liquids was altered, so the optical and acoustic beams were refracted simultaneously to the same angle. Using real-time feedback of PA A-line signals, the autofocusing probe adjusted the focus to maximize the PA amplitude and, thereby, increased the SNR at deeper depths compared to fixed-focus scanning.

Ma *et al.* investigated the use of OR-PAM to measure the melanin component of café-au-lait macules (CALMs) in patients^[116]. The researchers developed a fast linear confocal scanning PA dermoscopy (FLCS-PAD) system, in which a dual PVDF transducer created a laterally elongated acoustic focal field (~0.8 mm longitudinally × 3 mm laterally), and the optical focus was linearly scanned within the field using a two-axis galvanometer scanner. The optical depth-of-focus was about 150 μm, which included the epidermal layer well, and enabled reliable quantitative PA measurement in relatively uniform optical and acoustic fields. FLCS-PAD scans of healthy volunteers with two different skin colors showed that the PA amplitudes of SC and SB were higher in dark skin than in light skin. Then a patient with CALM was scanned before and after Q-switched ruby laser treatment, and the epidermal thickness and the melanin concentration were compared. The CALM area had slightly thicker epidermal thickness and significantly higher melanin concentration than the normal skin area, and the treatment only reduced the melanin concentration. The researchers suggested a PAINX score proportional to the epidermal thickness and melanin concentration; the score agreed well with the conventional melanin index measured from digital photographs.

A multiscale confocal PA dermoscopy (MC-PAD) system has been developed using multiple objectives (e.g., 4×, 10×, and 20×) to observe features in CALM and PWS patients^[117]. Increasing the magnification (i.e., NA) by the objective lens refined the resolution for visualization of skin structures, at the cost of reduced imaging depth. Thus, the SC, SB, and dermal layers were imaged using 20×/0.55NA, 10×/0.3NA, and 4×/0.1NA, respectively. The acoustic frequency of the PA signal was divided into different bands in the range of 5 to 90 MHz to optimize the visualization of skin layers. Quantitative results showed higher melanin concentration and thicker SB thickness in CALM-afflicted areas than in normal areas. The PWS study showed that the diameter and density of dermal vessels were greater in PWS areas than in normal areas. PAD analysis on PWS before and after photodynamic therapy (PDT) demonstrated that the diameter, depth, and density of lesion vessels were reduced after PDT but that the improvements were more significant in superficial dermis than in deep dermis^[100].

Wang *et al.* introduced bifocal dual-wavelength (532 and 1064 nm) PAM to improve the visualization of deep dermal vessels in PWS patients (Fig. 7)^[118]. The conventional 532 nm wavelength could visualize the epidermis and superficial vascular plexus, and the additional 1064 nm wavelength enabled tissue visualization up to ~3 mm depth, which includes the deep vascular plexus and hypodermis. The lateral resolutions were 6.6 μm for 532 nm and 46.8 μm for 1064 nm, and their foci were 1.5 mm apart in depth. The epidermal melanin density was lower in PWS than in normal skin, due to abnormal expansion of dermal vessels in PWS. The superficial dermal vessels were significantly increased to about four times that of normal skin, and deep dermal vessels had more branches to transport

nutrition to the superficial dermis in PWS than in normal skin. Further, the overall vascular diameter in the superficial dermis tended to be thicker in PWS than in normal skin.

A commercially available PAM system (PASONO-SKIN, Guangdong Photoacoustic Technology Co., Ltd., Foshan, China) has been used to classify melasma by quantifying the clinical indicators for melanin and blood vessels^[119]. The PASONO-SKIN system consists of a 532 nm nanosecond pulsed laser and a ring US transducer (center frequency: 35 MHz, bandwidth: 114%, focal length: 8 mm) and achieves a resolution of 50 μm axially and 7 μm laterally. The conventional classification of melasma has been complex due to various mixtures of pigment abnormalities and vascular formation. In this aspect, PAM measurements on the depth of melanin, mean vascular diameter, and vascular density were used to classify the melasma lesions quantitatively. The depth of melanin determined whether the lesion is the epidermal type (melanin only in the epidermis) or mixed (melanin in both epidermis and dermis), and the two vascular parameters further classified the lesions into M + V (i.e., increased vasculature) or M types (i.e., non-significant increase in the vasculature). PAM provided 3D structure data of melanin and blood vessels in the epidermis and dermis [Fig. 8(a)], and the images were quantified into the PA amplitude (arbitrary units, a.u.) of melanin and mean diameter (μm) and density (%) of vessels. As classified by the metrics, all types of lesions had a significant increase in the PA amplitude of melanin, but only the M + V type showed a significant increase in the vascular diameter and density [Fig. 8(b)]. The results showed that PAM could provide quantitative parameters for classifying melasma type.

4.2. Clinical PAMs Techniques for Imaging Skin Vasculature and Pigmentation

He *et al.* showed that FRSOM can distinguish melanoma lesions from benign nevi by quantifying differences in vascular density, complexity, and tortuosity between the two types of lesions^[120]. FRSOM images (Fig. 9) distinguish small vasculature from large vasculature structures by reconstructing data from two frequency bands: high frequency (40–120 MHz, Fig. 9, green) and low frequency (10–40 MHz, Fig. 9, red). The FRSOM system showed that an irregular dermal vasculature appears in the tumor area and is resolved in the edge of the lesion. However, to separate the effects of the melanin signal, the boundaries must be segmented. Therefore, the authors implemented dual-wavelength (515 and 532 nm) FRSOM to separate the melanin and Hb using spectral unmixing. The dual-wavelength FRSOM took about 25 s to scan an area of 4 mm × 2 mm and provided vascular features without having to segment the boundaries.

When the goal is to distinguish signals from multiple chromophores, a multi-wavelength laser must be used. Berezhnoi *et al.* developed ultrawide spectrum and bandwidth raster scan photoacoustic mesoscopy (UWSB-RSOM) to visualize the biomolecules in human skin using a laser that has a broad spectral range from visible to short-wave infrared (SWIR) [Fig. 10(a)]^[121]. The UWSB-RSOM system used an Nd:YAG OPO laser to generate $\lambda = 650, 1210, \text{ and } 1450 \text{ nm}$ and fast single-wavelength lasers that operated at 515 and 532 nm. The system had two focused transducers with center frequencies of 55 and 23.9 MHz. The scan with fast single-wavelength lasers and the 55 MHz transducer had spatial resolutions of 8.6 μm axially and 29.6 μm laterally. The scan with the SWIR

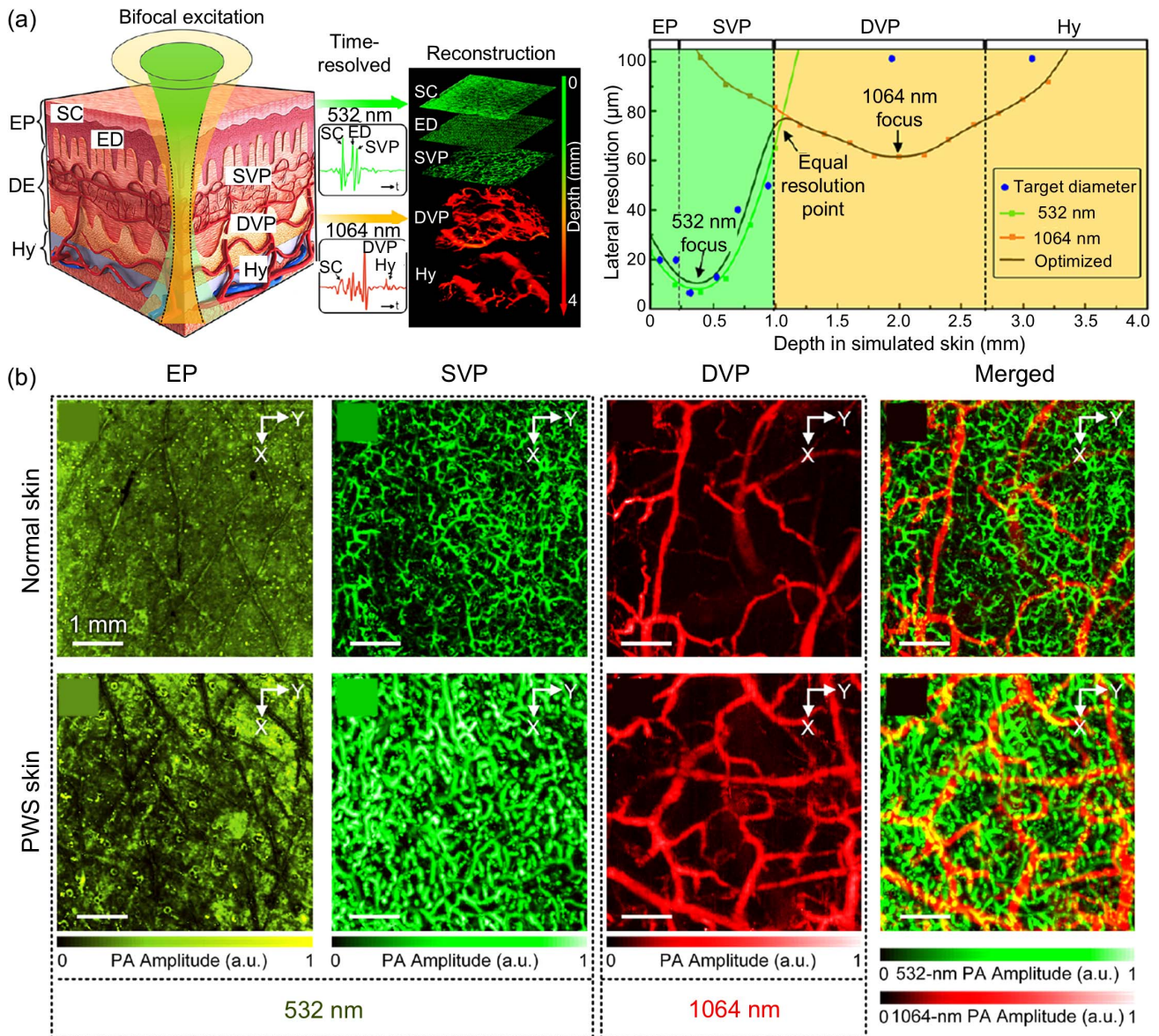


Fig. 7 Bifocal dual-wavelength PAM technique for port wine stain (PWS) characterization. (a) Two optical wavelengths, 532 and 1064 nm, were focused at different depths and superposed to provide elongated focal zone and deep imaging depth up to 3 mm. The epidermis (EP) and superficial vascular plexus (SVP) were imaged at 532 nm and deep vascular plexus (DVP) at 1064 nm. (b) Compared to normal skin, PWS skin expressed less melanin in the EP layer and more vasculature in the SVP and DVP layers. DE, dermis; Hy, hypodermis; SC, stratum corneum; ED, epidermal-dermal junction; PWS, port wine stain; PA, photoacoustic; and a.u., arbitrary unit. The figures were reproduced with permission from Ref. [118] (Copyright © 2021 European Academy of Dermatology and Venereology).

laser and 23.9 MHz transducer had spatial resolutions of 33 μm axially and 53 μm laterally. Scans of forearm skins of two healthy volunteers obtained high-resolution images of subcutaneous fat, sebaceous glands, hair follicles, and microvasculature. UWSB-RSOM distinguished between melanin and melanoidins in the epidermis, identified lipid distributions in the SWIR range, and visualized water content at 1450 nm [Fig. 10(b)]. The UWSB-RSOM can visualize the skin's molecular composition, including hairs that extend from the subcutaneous fat to the skin surface and beyond.

4.3. Clinical PAT Techniques for Imaging Skin Vasculature and Pigmentation

Much PAT research to image joint vasculature and pigment has targeted diagnosis of melanoma, which is a malignant tumor caused by the transformation of melanocytes, and that accounts for most deaths from skin cancer. A person with melanoma is most likely to survive when diagnosis is early and treatment is performed before the melanoma metastasizes. To identify the progression stage (according to the Breslow depth), the size

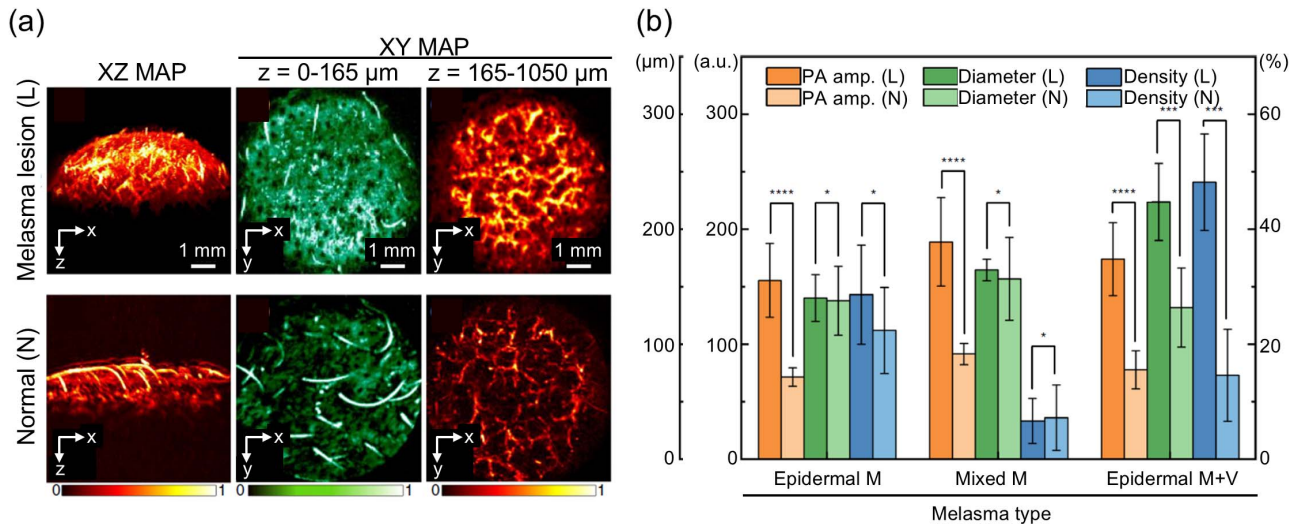


Fig. 8 Classification of melasma lesion types using PAM. (a) The PAM images are from a patient with epidermal M + V type melasma, showing denser melanin in the epidermal layer ($z = 0-165 \mu\text{m}$) and denser and thicker vessels in the dermal layer ($z = 165-1050 \mu\text{m}$). (b) All types of melasma lesions showed a significant increase in the PA amplitude of melanin. The vascular diameter and density were not significantly changed in the epidermal M and mixed M types, but the M + V type had a significant increase in the two vascular metrics. MAP, maximum amplitude projection; a.u., arbitrary unit; and PA, photoacoustic. The figures were reproduced with permission from Ref. [119] (Copyright © 2023 by the authors).

and thickness of melanoma lesions must be quantified, and lesions must be treated or excised. Melanoma lesions contain high concentrations of melanin that produce a significantly stronger PA signal against normal skin and, therefore, can be distinguished from surrounding tissue.

Breathnach *et al.* used a commercial Vevo LAZR (VisualSonics Inc., Toronto, Canada) system with LZ 550 probe

(VisualSonics Inc., Toronto, Canada) to scan melanomas^[122]. The system includes a 256-element linear array transducer with a high center frequency of 40 MHz. A tunable OPO laser (680–970 nm, OPOTEK, Carlsbad, USA) can be used with a fiber bundle to irradiate the laser from both sides of the transducer array at 30° to the imaging plane. $\lambda = 680 \text{ nm}$ was selected for single-wavelength PA scans, and five wavelengths

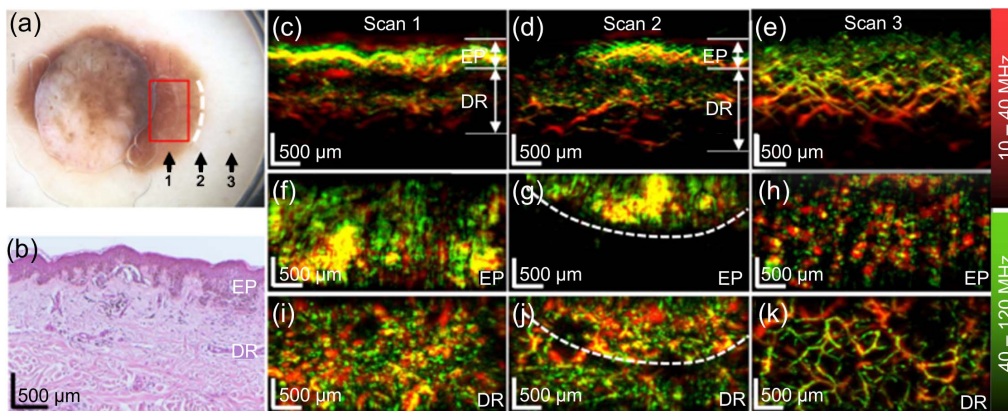


Fig. 9 RSOM images of a melanoma lesion and the surrounding skin tissue. (a) A photograph of a melanoma lesion. Arrows indicate the three scanning positions. The red rectangle depicts the FOV of 4 mm × 2 mm. (b) Histological images of the melanoma sample corresponding to the area with label 1 in (a). (c)–(e) Cross-sectional RSOM images of the three scanned regions [labels 1, 2, and 3 in (a)]. (f)–(h) Maximum amplitude projection (MAP) images corresponding to the epidermal (EP) layer of (c)–(e). (i)–(k) MAP images corresponding to the dermal (DR) layer of (c)–(e). The white dashed lines in (g) indicate the boundary between the pigmented lesion and the surrounding skin tissue. Comparing the dermal vascular structures of (i)–(k), a dense dotted vascular pattern is clearly visible in the tumor base area. The figures were reproduced with permission from Ref. [120] [Copyright © 2022 by the author(s)].

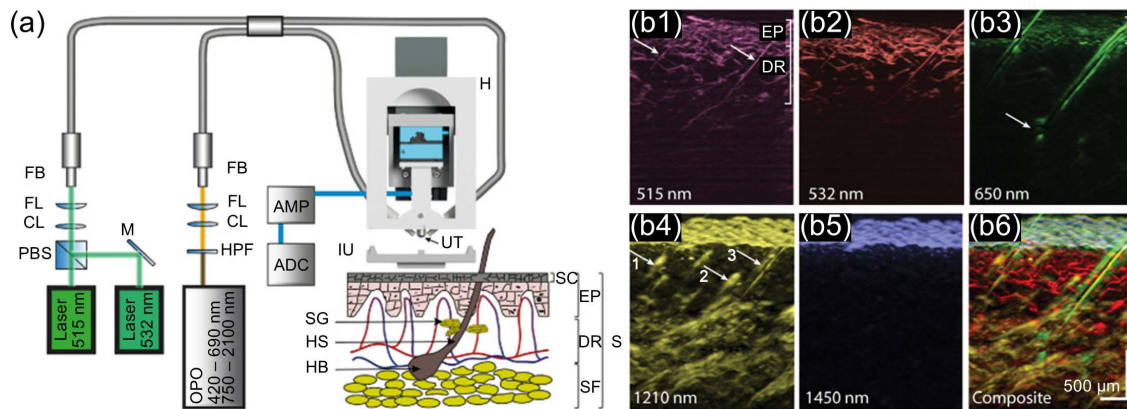


Fig. 10 UWSB-RSOM system configuration and cross-sectional USWB-RSOM images over 5 wavelengths. (a) Schematic of UWSB-RSOM and a structure of the imaging target (skin). (b1)–(b6) Cross-sectional RSOM images of skin over 5 wavelengths. (b1), (b2) Distribution of hemoglobin and melanin in the skin at 515 and 532 nm. Arrows indicate the position of hair. (b3) Melanin in the epidermis and hair at 650 nm. (b4) Subcutaneous fat, sebaceous glands (marked with arrows 1 and 2), and water content in the epidermis at 1210 nm; arrow 3, sebum content on the hair shaft. (b5) Water distributed in the epidermis at 1450 nm. (b6) Composite of images at all five wavelengths. ADC, analog-to-digital converter; AMP, 60 dBm amplifier; CL, collimating lens; D, dermis; EP, epidermis; FB, fiber bundle; FL, focusing lens; H, UWSB-RSOM holder; HPF, high-pass filter; HS, hair shaft; HB, hair bulb; IU, detachable interface unit; M, mirror; PBS, polarizing beam splitter; S, schematic of human skin; SF, subcutaneous fat; SG, sebaceous glands; UT, ultrasound transducer. The figures were reproduced with permission from Ref. [121] (Copyright © 2019 Optical Society of America).

(680, 700, 750, 850, and 900 nm) were used for spectral unmixing to distinguish melanin from other chromophores in the tissue. The full multi-wavelength scanning procedure took about 7 min. The PAT images clearly demarcated the location of the melanoma lesion and identified its depth [Figs. 11(a)–11(c)], and both single and multi-spectral PAT presented high correlation coefficients (0.98 for benign and 0.99 for melanoma) with histological thickness. However, PAT measurement overestimated melanoma thickness in all cases, mainly because of shrinkage caused by dehydration of the excised sample during histologic sectioning^[123]. Further, multi-spectral PAI effectively visualized the lesion. The *in vivo* images were not perfectly matched with the histology results and, thus, had large measurement errors.

Kim *et al.* imaged an excised melanoma skin sample using a clinical PA/US imaging system that combines a clinically viable research US system (ECUBE-12 R, Alpinion Medical Systems, Anyang, Korea) and an OPO laser (Phocus Mobile, OPOTEK, Carlsbad, USA) to generate three wavelengths (680, 800, and 1064 nm)^[124]. To image the whole lesion, a linear motorized scanning system moved the imaging probe along the elevation direction and then stacked cross-sectional PAT images. The spatial resolutions were 0.2 mm axially and 1.2 mm laterally, and the scanning range was 38.1 mm × 75 mm. The PA MAP image melanoma lesion boundary was acquired from displayed areas of melanoma that are not visible to the naked eye, and the thickness from the PA image was consistent with the histopathological result. A follow-up study used the same clinical PA/US imaging system to image melanoma lesions on patients *in vivo*^[125]. The authors used a lightweight (<1 kg) handheld probe scanner, which provided versatile 3D PAT imaging on various locations of melanoma lesions on patients *in vivo*.

The FOV was 38.1 mm × 31.4 mm, and the imaging depth was up to 30 mm; data acquisition took about 57 s for multi-wavelength imaging using five wavelengths (700, 756, 796, 866, and 900 nm). Both single (700 nm) and multi-wavelength PA images identified the melanoma lesion boundary in 3D and provided its depth information [Figs. 11(d)–11(h)]. The lesion depth measured from PAI agreed well with histology, but the histopathological depth values were smaller than PAI depth values due to the dehydration and shrinkage of samples after excision. As a special case, they clearly visualized feeding blood vessels near a suspected melanoma in a patient who refused surgery.

PAT has also been evaluated for diagnosis of non-melanoma skin cancers (NMSCs), which constitute most skin cancers. The lesions infiltrate skin tissue to uneven depths, and their boundaries can be difficult to identify, so these carcinomas are treated using Mohs micrographic surgery, which performs repeated excision and examination. This consumes much time, so the boundary and the size of the lesion must be estimated accurately before the surgery.

Kukk *et al.* modified their integrated OCT-Raman spectroscopy device to perform PA imaging. The modified system uses a single-crystal US transducer (L22-14vX-LF, Vermon, France) that includes 128 elements with a central frequency of 18 MHz^[126]. An OPO laser (SpitLight Compact 400 OPO, InnoLas Laser GmbH, Germany) emits maximal pulse energy at 430 nm wavelength with 7 ns pulse duration and 20 Hz repetition. This system had resolutions of 200 μm axially and 100 μm laterally for US, and 300 μm axially and 200 μm laterally for PA, with a PA imaging depth of up to 5 mm. *In vivo* tests on human skin nevi demonstrated a good correlation between PA measurements and histological results [Fig. 12(a)], although tissue shrinkage or

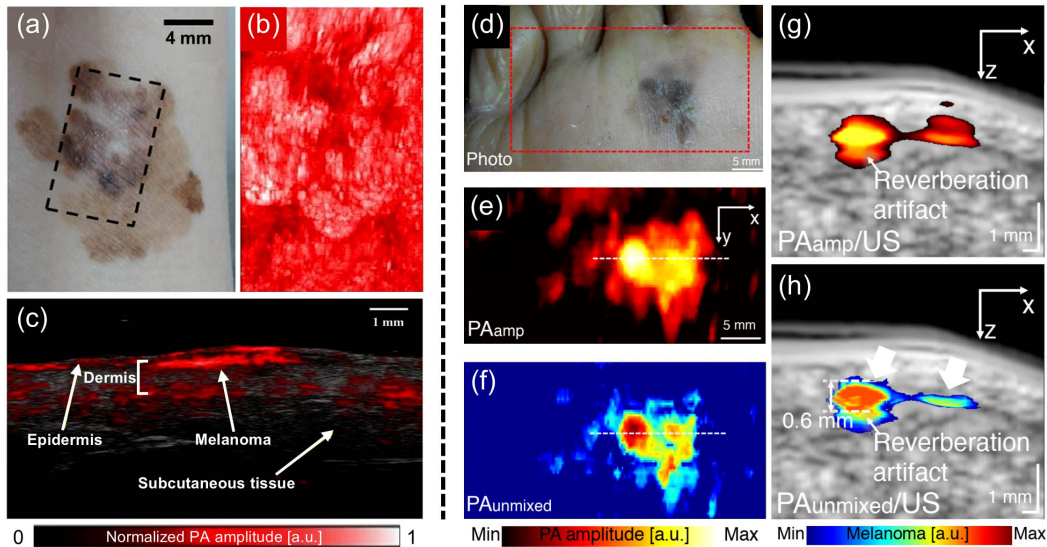


Fig. 11 PAT techniques for melanoma imaging. (a) Clinical photograph of a melanoma. (b) 3D PA scan image of the black dashed region in (a). (c) Co-registration of PA and B-mode US images of *in situ* melanoma on the upper left extremity. (d) Clinical photograph of an *in situ* type of melanoma. (e) PAampMAP and (f) PAunmixedMAP images of the red dashed region in (d). (g) PAamp/US overlaid and (h) PAunmixed/US overlaid B-scan images from the white dashed lines in (e) and (f). PA, photoacoustic; US, ultrasound; PAamp, PA amplitude; PAunmixed, PA unmixed melanoma; MAP, maximum amplitude projection. The figures were reproduced with permission from Refs. [122] (Copyright © by the authors) and [125] (Copyright © 2020 European Academy of Dermatology and Venereology).

position-matching errors caused differences between the thickness measurements by histology and by PAI. The authors also imaged skin lesions that were suspected to indicate skin cancers^[127]. PA/US image measurements of lesion thickness correlated strongly ($R^2 = 0.93$) with histological measurements, especially for lesions that had histological thickness between 0.2 and 3 mm. These results show the potential of PAT to assist in determining the extent of excision and improve the accuracy at which skin cancers can be diagnosed.

Attia *et al.* imaged skin lesions suspected to be non-melanoma carcinomas using an *inVision* 512-echo MSOT system (*iThera Medical GmbH*, Munich, Germany)^[128]. The FOV of the system was 10 mm × 10 mm × 12 mm and achieved a nearly isotropic resolution of 80 μm, which allowed precise measurement of the tumor dimensions. Ten optical wavelengths (700, 715, 730, 760, 780, 790, 800, 825, 850, and 900 nm) were used for multi-spectral measurement, and the whole imaging procedure took about 5 min per patient. Tumor dimensions measured using the MSOT system correlated well with histological measurements (intraclass correlation coefficient is >0.7). Also, the system could provide vascular features of non-melanoma skin tumors. Chuah *et al.* used MSOT for a further study of different types of NMSCs on different skin phototypes^[129]. Dimensions of the NMSCs could be precisely imaged regardless of the skin phototype because MSOT can distinguish melanin from HbO₂ and HbR. Measurements of shallow tumors near the skin surface showed relatively large errors, but the overall results from the study showed that the depth estimated using PAI agreed well with the histology results. These results indicate that PAI has the potential to increase the precision of tumor ablation and to decrease the recurrence rates of NMSCs.

PAI can also be used to differentiate between benign and malignant skin tumors, by exploiting its ability to distinguish between blood vessels and melanin. For instance, skin tags are commonly benign skin lesions, but they can be malignant lesions like squamous cell carcinoma, BCC, or melanoma. Therefore, a sensitive diagnostic modality is needed to distinguish the malignant lesions accurately. Fredman *et al.* evaluated reflectance confocal microscopy (RCM), OCT, and MSOT to analyze skin tags to provide lesion dimensions and micromorphological distributions of vascularization and melanin^[130]. The MSOT imaging used MSOT Acuity (*iThera Medical GmbH*, Munich, Germany), in which the US transducer array had 256 elements with 8 MHz central frequency and optical wavelengths of 700, 730, 760, 780, 800, 850, and 875 nm. The FOV was 15 mm × 15 mm × 20 mm, and each scan took about 5 s. Histopathological analysis and dermoscopy measurements commonly detected no malignancy in all lesions, and all three imaging methods also showed features that correspond to benign lesions. OCT and RCM gave detailed information mainly about vessel distribution and the nest of melanocytes, respectively, but MSOT provided integrated information about both features. Blood vessels located below the melanin signal were clearly distinguished by their HbO₂ signal; this result indicates that melanin was not present in the lower layer of the dermis. Von Knorring *et al.* added high-frequency ultrasound (HFUS) imaging to RCM, OCT, and MSOT, and imaged patients that had either benign or malignant tumors^[131]. PAI found abundant blood vessels inside most of the malignant tumors; this result indicates that the malignancy of the lesion was closely associated with the converging network of blood vessels and melanin [Fig. 12(b)].

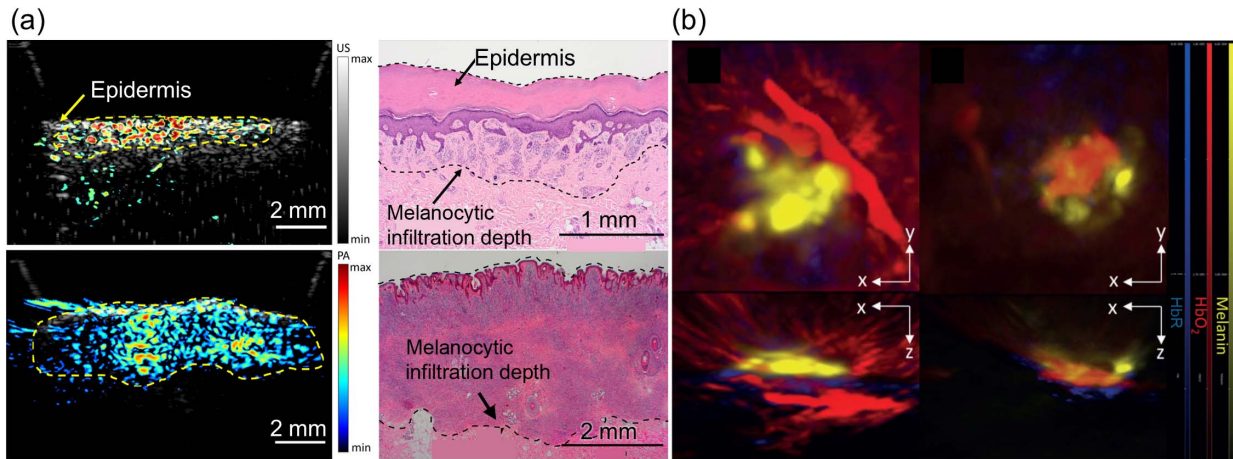


Fig. 12 PAT techniques for skin lesions. (a) Comparison of combined *in vivo* US/PA measurement on human nevi (left) and the corresponding histological measurements (right). (b) PA imaging of nevus with atypical proliferation (left) and basal cell carcinoma (right). The nevus presents chaotic and prominent blood vessels outside the melanin area (yellow), HbO₂ (red), and Hb (blue) blood vessels with enlarged diameter. The carcinoma shows abundant HbO₂ signal (red) inside the melanin area, demonstrating a converging network of melanin (yellow), HbO₂ (red), and HbR (blue). PAT, photoacoustic tomography; US, ultrasound; PA, photoacoustic; HbO₂, oxy-hemoglobin; HbR, deoxy-hemoglobin. The figures were reproduced with permission from Refs. [126] [Copyright © 2023 by the author(s)] and [131] (Copyright © 2022 Acta Dermatovenereologica).

5. Discussion

In the papers reviewed here, both imaging depth (Fig. 13, left) and lateral FOV (Fig. 13, right) show a trade-off relationship with spatial resolution. Least squares line fitting showed an imaging depth of $\approx 92.6 \times$ spatial resolution, which agrees with previous reports^[69,132]. Similarly, lateral FOV $\approx 236 \times$ spatial resolution. These relations can provide guidance on

selecting an appropriate PAI modality for the skin imaging application of interest, depending on the desired precision and the size of the target.

Systems for skin imaging have a range of specifications PAM (Table 1), PAMes (Table 2), and PAT (Table 3). Generally, PAM and PAMes offer much higher axial/lateral resolutions (~ 5 to $50 \mu\text{m}$) than PAT ($\sim 200 \mu\text{m}$). PAM can be implemented

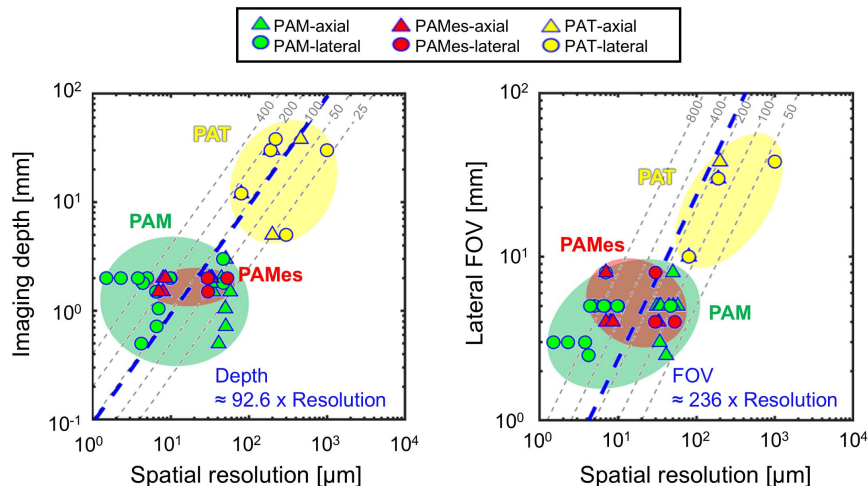


Fig. 13 Specification plots relating the spatial resolution, imaging depth, and lateral FOV of clinical PA skin imaging systems. The overall relationship of the imaging depth versus spatial resolution (left) and the lateral FOV versus spatial resolution (right) is presented. Dotted lines show reference trade-off lines with a given ratio, and the blue dotted line is obtained from least-square fitting including both axial (triangle marker) and lateral (circle marker) resolutions. PAM, photoacoustic microscopy; PAMes, photoacoustic mesoscopy; PAT, photoacoustic tomography; FOV, field of view; PA, photoacoustic. (Refs. PAM- [95,97,99,100,114–119]; PAMes - [101,102,104,107,108,120,121]; PAT - [110,113,125–127,129].

Table 1 Specifications of PAM Systems for Clinical Skin Imaging.

Ref.	Modality	Laser wavelength (nm)	US transducer	US frequency	FOV, lateral x elevation x axial (mm x mm x mm)	Spatial resolution (μm)	Scan time
[95]	OR-PAM	532	Focused	Center: 40 MHz BW: 110%	5 × 5 × 2	Lateral: 5 Axial: 31.2	~0.1 s per B-scan
[96]	OR-PAM + PPG	532	Flat ring transducer	Center: 15 MHz	Lateral: 1 Axial: 1	Lateral: 2.5 Axial: 68.4	0.02 s per B-scan
[97]	OR-PAM + USM	532	Dual (coaxial annular, outer-PZT, inner-PVDF), focused	US excitation (PZT) Center: 33.4 MHz BW: 19.5–47.2 MHz PA/US reception (PVDF) Center: 35 MHz BW: 11.8–58.2 MHz	Lateral: ~5 × 5 Axial: 1.5 (PA), 5 (US)	Lateral: 45 (US), 6.8–7.1 (PA) Axial: 57.8 (US)	NA
[98]	OR-PAM + Deep learning	532	Focused	Center: 20 MHz, BW: 100%	5 × 5 × 4	NA	NA
[99]	Bessel-beam OR-PAM	532	Focused ring transducer	Center: 40 MHz BW: 120%	5 × 4 × 1.5	Lateral: 6.5 (1 mm DOF) Axial: 35	NA
[100]	OR/AR-PAM	532	Focused annular PVDF	Center: 42 MHz	5 × 5 × 2	Lateral: 10–40 (0.2–1.5 mm depth) Axial: 34	3–5 min per C-scan
Vasculature and pigmentation imaging							
[114]	Switchable OR/AR-PAM	532	Focused	Center: 45 MHz BW: 7–83 MHz	5 × 3 × 1.8	Lateral: 4.4 (OR), 47 (AR) Axial: 35	0.5 s per B-scan, ~2.5 min per C-scan
[115]	Switchable OR/AR-PAM	532	Autofocusing PVDF-based transducer	Center: 32.8 MHz BW: 45.4 MHz	5 × 5 × 2	Lateral: 9.8 (OR, variable with the applied voltage) Axial: ~44.6	NA
[116]	OR-PAM	532	Focused PVDF	BW: 10–75 MHz	2.5 × 2.5 × 0.5	Lateral: 4.2 Axial: 41	~1 s per B-scan
[117]	OR/AR-PAM	532	Focused annular PVDF	Center: 45 MHz BW: 5–85 MHz	3 × 3 × 2	Lateral: 3.8, 2.3, 1.5 (for 4x, 10x, 20x objective lens) Axial: 34	NA
[118]	Dual-wavelength bifocal OR-PAM	532, 1064	Focused ring transducer	Center: 30 MHz	Lateral: 5 × 5 Axial: 0–0.72 (532 nm), 0.72–3 (1064 nm)	Lateral: 6.6 (532 nm), 46.8 (1064 nm) Axial: 50.6	NA
[119]	Commercially available PAM (PASONO-SKIN)	532	Ring transducer	Center: 35 MHz BW: 114% (15–55 MHz)	~8 × 8 × 1.05	Lateral: 7 Axial: 50	NA

Notes: PAM, photoacoustic microscopy; US, ultrasound; FOV, field of view; OR, optical resolution; BW, bandwidth; PPG, photoplethysmography; USM, ultrasound microscopy; PZT, lead zirconate titanate; PVDF, polyvinylidene fluoride; PA, photoacoustic; NA, not available; AR, acoustic resolution.

Table 2 Specifications of PAMes Systems for Clinical Skin Imaging.

Ref.	Modality	Laser wavelength (nm)	US transducer	US frequency (MHz)	FOV, lateral x elevation x axial (mm x mm x mm)	Spatial resolution (μm)	Scan time
[101]	RSOM	532	Focused transducer	Center: 55 BW: 10–120	4 x 2 x 1.5	Lateral: 30 Axial: 8	70 s per C-scan
[102]	RSOM	532	Focused transducer	Center: 55 BW: 10–120	8 x 2 x 1.5	Lateral: 30, Axial: 7	80 s per C-scan
[104]	RSOM	532	Focused transducer	Center: 55 BW: 10–120	4 x 2 x 2	Lateral: 30, Axial: 8	70 s per C-scan
[107]	RSOM	532	Focused transducer	Center: 55 BW: 10–120	4 x 2 x 2	Lateral: 30 Axial: 8	70 s per C-scan
[108]	FP-RSOM	532	Focused hole transducer	Center: 50 BW: 10–120	4 x 2 x 1.5	Lateral: 30 Axial: 7 (same as RSOM)	~1s per B-scan 15 s per C-scan
[120]	FRSOM	532, 555, 579, and 606	Focused hole transducer	Center: 50 BW: 10–120	4 x 2 x 1.5	Lateral: 30 Axial: 7 (same as RSOM)	15 s (single) 60 s (multi) per C-scan
[121]	UWSB-RSOM	650, 1210, 1450, 515, and 532	Two spherically focused piezoelectric transducers	Center: 23.9, 55	Lateral: 4 Axial: 2	At 23.9 MHz Lateral: 53 MHz Axial: 33 At 55 MHz Lateral: 29.6 Axial: 8.6	<2 min per scan

Notes: PAMes, photoacoustic mesoscopy; US, ultrasound; FOV, field of view; BW, bandwidth; RSOM, raster-scan photoacoustic mesoscopy; FP-RSOM, fast raster-scan photoacoustic mesoscopy; FRSOM, fast raster-scan photoacoustic mesoscopy; UWSB-RSOM, ultrawide spectrum and bandwidth raster-scan photoacoustic mesoscopy.

Table 3 Specifications of PAT Systems for Clinical Skin Imaging.

Ref.	Modality	Laser wavelength (nm)	US transducer	US frequency	FOV, lateral x elevation x axial (mm x mm x mm)	Spatial resolution (μm)	Scan time
[110]	MSOT	700 to 850	Linear array transducer	Vasculature imaging Center: 4 MHz BW: 52%	Lateral: 30 mm Axial: 30 mm	~190	NA
[112]	MSOT	NA	NA	NA	15 x 15 x 15	NA	NA
[113]	LED based PAI	850	Linear array transducer	Center: 9 MHz	Axial: 38 mm ^a	Lateral: 460 ^a Axial: 220 ^a	20 s per B scan 1–3 min per C-scan
Vasculature and pigmentation imaging							
[122]	PAISU	680, 700, 750, 850, and 900	Linear array transducer	Center: 40 MHz BW: 55%	NA	NA	~3 min (single) ~7 min (multi) per C-scan
[125]	PA/US	700, 756, 796, 866, and 900	Linear array transducer	Center: 8.5 MHz BW: 3–12 MHz	38.1 x 31.4 x ~30	Lateral: 1000 Axial: 200	~11.4 s (single) ~57 s (multi) per C-scan
[126]	PA/US	430	Single crystal transducer	Center: 18 MHz BW: 67%	Axial: 5	Lateral: 300 Axial: 200	<1 s per B-scan
[127]	PA/US	Single: 430 or 530	Single crystal transducer	Center: 18 MHz BW: 67%	Axial: 5	Lateral: 300 Axial: 200	<50 s per C scan
[128]	MSOT	NA	NA	NA	NA	NA	NA
[129]	vMSOT	700, 715, 730, 760, 780, 790, 800, 825, 850, and 900	Spherical matrix array transducer	NA	10 x 10 x 12	80 (isotropic)	~5 min per C scan
[130]	OCT, RCM, and MSOT	700, 730, 760, 780, 800, 850, and 875	Hemispherical array transducer	Center: 8 MHz BW: 60%	15 x 15 x 20	NA	~5 s per C scan
[131]	HFUS, RCM, OCT, and PAI	NA	NA	NA	15 x 15 x 20	NA	NA

^aParameters are from Xia et al.^[133]

Notes: PAT, photoacoustic tomography; US, ultrasound; FOV, field of view; MSOT, multi-spectral photoacoustic tomography; BW, bandwidth; NA, not available; LED, Light Emitting Diode; PAI, photoacoustic imaging; SU, spectral unmixing; PA, photoacoustic; vMSOT, volumetric MSOT; OCT, optical coherence tomography; RCM, reflectance confocal microscopy; HFUS, high-frequency ultrasound.

Table 4 PAI Analysis Features of the Skin Vasculature.

Ref.	Imaging target	Analysis metrics	Key features & findings
[95]	Volunteer's opisthenar and palm areas	PAM Visual assessment of the number of capillaries, depth distribution, and vessel diameter	Imaging depth was greater in the palm than in the opisthenar due to higher melanin concentration in the epidermis
[96]	Volunteer's finger	Vascular movements and changes in the blood volume	The vascular movements and the heartbeat rates measured with both OR-PAM and PPG well matched between the two modalities
[97]	Volunteer's palm	PA: Epidermal (0–90 μm), epidermal-dermal junction (90–210 μm), dermis (210–350 μm), and vessel plexus (350–1500 μm). US: big vessel (1.5–2.6 mm) and fibrous tissue (2.6–5 mm)	The PA and US microscopic images characterized the microvasculature information and full structures of skin <i>in vivo</i> , respectively
[98]	Volunteer's palm	Axial resolution and deep vessel visibility	Deep learning model improved the epidermal layer differentiation and visibility of deep vessels
[99]	Traumatized skin	SC layer thickness and PA amplitude, SB layer PA amplitude, and dermal vessel diameter	Increased thickness and PA amplitude in the SC layer, disappearance of signals in the SB layer, and development of small and dense microvasculature in the dermal layer
[100]	PWSpre- and post-PDT treatment	Density, depth, and diameter of dermal vessels	Density, depth, and diameter of lesion vessels were reduced after PDT where the effects were more significant in superficial dermis than in deep dermis
[101]	Allergic and irritant skin reactions in patch testing	PAMes Blood volume, vessel fragmentation, and frequency content ratio	Allergic reactions showed higher vessel fragmentation and lower frequency ratios compared to irritant reactions
[102]	UV radiation region in volunteers' skin	Vessel visibility and vessel diameter	RSOM imaging revealed UV-induced recruitment of previously non-perfused vessels and vasodilation, visible as an increase in vessel diameter
[104]	Patient with moderate atopic dermatitis	Epidermis thickness, total blood volume, and vessel diameter	32% reduction in epidermis thickness, 10% decrease in total blood volume, and 26% reduction in vessel diameter post-treatment
[107]	Pretibial region of the participants with diabetes mellitus and age-matched healthy volunteers	Epidermal thickness, signal density of epidermis layer, dermal blood volume, vessel diameter, small vessel number, and large vessel number	The analysis revealed significant differences in microvascular parameters between healthy individuals and diabetes patients, with smaller vessels (<40 μm in diameter) showing the most marked differences
[108]	Healthy individuals, smokers, and CVD patients	Vessel diameter, blood volume, and vessel density	Significant differences in microvascular ED biomarkers among healthy individuals, smokers, and CVD patients, providing a novel tool for early diagnosis and monitoring of cardiovascular risks

	PAT	
[110]	Fingers of patients with SSc and healthy volunteers	HbR, HbO ₂ , and HbT
[112]	Healthy ventral forearm with RH	HbO ₂ , HbR, HbT, and mSO ₂
[113]	Patients with facial PWS	“PWS level,” indicating the severity of PWS lesions
		Assessing microvascular dysfunction in SSc. Patients with progressive SSc had significantly lower MSOT values compared to patients with stable disease and healthy volunteers
		PAT observations of the RH identified superficial and deeper vascular structures parallel to the skin surface as part of the human skin vascular plexus. PAT revealed that the suprasystolic occlusion impacts both plexus differently
		The decrease in PWS levels after treatment based on PAI-association indicates better repeatability in assessing response to treatment compared to dermatologist-assigned clearance scores. It is a new quantitative assessment method for PWS severity and treatment response

Notes: PAI, photoacoustic imaging; OR-PAM, optical resolution photoacoustic microscopy; PPG, photoplethysmography; PA, photoacoustic; US, ultrasound; SC, stratum corneum; PA, photoacoustic; SB, stratum basale; PWS, port-wine stains; PDT, photodynamic therapy; UV, ultraviolet; RSOM, raster-scan optoacoustic mesoscopy; CVD, cardiovascular disease; ED, endothelial dysfunction; SSc, Systemic sclerosis; RH, reactive hyperemia; HbO₂, oxy-hemoglobin; HbR, deoxy-hemoglobin; HbT, total hemoglobin; mSO₂, MSOT-derived oxygen saturation; MSOT, multi-spectral optoacoustic tomography.

in either OR-PAM or AR-PAM, depending on the location of optical and acoustic foci. OR-PAM uses a focused light beam to achieve the best lateral resolution (~7 μm), which achieves detailed imaging in the epidermal layers (SC, SB) and superficial dermal layer. To image deep vasculature in the dermal layer, OR-PAM and AR-PAM are often used switchably, or dual-wavelength 532/1064 nm foci can be used.

AR-PAM techniques can be implemented with almost the same specifications as PAMes because they are both built on a US focus. However, PAMes systems, often known as RSOM, offer a fine axial resolution of <10 μm thanks to the ultrawide US bandwidth (~10 to 120 MHz) and can also distinguish vessel sizes by dividing the bandwidth range. Both PAM and PAMes can clearly identify the vasculature or melanin structures in each skin layer, but multi-wavelength laser excitation is not widely used.

Especially for PAM, the lateral resolution coarsens as the optical wavelength increases, so λ > 532 nm is not preferred. Thus, the signals of microvasculature are not distinguished from those of melanin spectrally but instead are distinguished to a certain extent by identifying the skin layer that they occupy. Instead, PAM can provide quantitative analysis of detailed skin structures such as the depth, diameter, and density of microvessels and, thereby, enables sensitive detection of abnormalities in the skin layers.

PAT has much coarser spatial resolution PAM or PAMes methods, but it allows large transverse scan areas (~30 mm × 30 mm) with imaging depth of <30 mm, whereas those of PAM and PAMes are limited to ~5 mm × 5 mm and <5 mm. Therefore, PAT cannot readily distinguish fine capillary structures, but vessels as small as arterioles or venules can be consistently identified, imaged, and analyzed to track changes. Furthermore, PAT systems usually deploy a wavelength-tunable laser source, so multi-wavelength measurements enable Hb to be distinguished spectrally from melanin chromophores. For example, MSOT systems provide quantitative measurement of functional biomarkers (e.g., HbR, HbO₂, and sO₂) using NIR excitation wavelength characteristics to each chromophore, thereby providing an objective and quantitative diagnosis of disease activities.

The three PAI modalities use different analysis metrics related to skin vasculature (Table 4) or vasculature plus pigment structures (Table 5). The differences in the diagnostic information can be summarized as follows: PAM and PAMes focus on analyzing the detailed micro-scale vascular or melanin structures layer by layer, whereas PAT focuses on measuring the dimensions of a whole lesion or relative concentrations of Hb or melanin. In skin diseases including allergies and atopy, accompanying superficial changes such as inflammatory reactions, PAM or PAMes could be useful for detecting changes in skin thickness and vascular structure and determining the effectiveness of treatments. They can also be used in other skin pigment disorders such as PWS to analyze and quantify the characteristic features of pigment and vasculature. For skin diseases with macroscopic lesions such as melanoma, it is important to assess a whole lesion dimension and determine whether a lesion is benign or not. In this sense, PAT can provide a full scan of an entire lesion for a holistic view of melanin and vessel distribution changes reaching the deep subcutaneous layer under the skin. It is relatively easy to apply multi-wavelength imaging, which can be used to specifically differentiate between melanin and vascular signals. The different analytic roles of PAI modalities

Table 5 PAI Analysis Features of the Skin Vasculature and Pigmentation.

Ref.	Imaging target	Analysis metrics	Key features & findings
[114,115]	Volunteer's opisthenar and palm areas	PAM Melanin concentration of the SC (0–100 μm) and the SB (100–200 μm), vascular density below the SB (200–2000 μm)	Melanin concentration was significantly smaller, and vascular density was higher in the palm skin than in the opisthenar skin
[116]	CALM before and after Q-switched ruby laser treatment	PA amplitude of the SC and SB, epidermal thickness, and melanin concentration of CALM patient	Melanin concentration and epidermal thickness were significantly higher in the CALM area than in normal skin. Melanin concentration was significantly reduced after laser treatment
[117]	CALM, PWS	CALM: melanin concentration, SB thickness; PWS: microvessel density, vascularization increase	CALM skin had a higher PA signal intensity and thicker SB than that of healthy skin. Dermal vessels had greater diameters and were denser in appearance in PWS skin than in healthy skin
[118]	PWS	Melanin density in epidermal layer, vessel density and diameter in superficial dermal, and deep dermal layers	In PWS, the epidermal melanin density was lower, the superficial dermal vessels were significantly increased, deep dermal vessels had more branches, and vascular diameter in superficial dermis tended to be thicker
[119]	Melasma	PA amplitude and depth of epidermal melanin, mean dermal vascular diameter, and mean dermal vascular density	The PA amplitude of the epidermis, mean vascular diameter, and density in lesional skin were significantly higher than that in non-lesional skin. Mean vascular diameter and density were important in classifying melasma types M and M + V
[120]	10 melanoma lesions and 10 benign nevi	PAMes Vascular density, complexity, and tortuosity	The FRMOM system effectively distinguished melanoma from benign nevi, providing valuable biomarkers for lesion characterization and improving diagnostic accuracy
[121]	Forearm skin of healthy volunteers	Fat, sebaceous glands, hair follicles, and microvasculature	UWB-RSOM distinguished between melanin and melanoidins in the epidermis, identified lipid distributions in the SWIR range, and visualized water content at 1450 nm
[122]	Patients with pigmented cutaneous lesions suspicious of melanoma	PAT Tumor thickness	The photoacoustically measured lesion thickness gave a high correlation with the histological thickness measured from resected surgical samples
[125]	Melanoma patients	Tumor depth	The 3D multispectral photoacoustic imaging not only provides well-measured depth and sizes of various types of melanomas but also visualizes the metastatic type of melanoma
[126]	Patient with skin nevi	Maximal nevi depth	Developed a single-head co-localized US/PAT imaging system allowing for structural and depth measurement with the application for non-invasive diagnosis of skin cancer. The C-mode measured dermal structure and melanocytic depth correlated well with the histology

[127]	Patients who had suspicious skin lesions identified by dermatologists as potentially indicative of skin cancer	Thickness of the lesion at its thickest position	The results procured in our study underscore the potential of combined ultrasound and photoacoustic tomography as a promising non-invasive 3D imaging approach for evaluating human nevi and other skin lesions
[128]	Patients presented with lesions suspicious of non-melanoma carcinomas	Lesion dimensions	The dimensions were then correlated from the measurements acquired from histology, showing a good correlation via the intraclass correlation coefficient
[129]	Patients with lesions suspicious of non-melanoma skin cancer	Tumor depth and length	A statistically significant correlation for both tumor depth and length was found between vMSOT and histologic analysis
[130]	Patients with skin tags	HbO ₂ , HbR, and melanin	MSOT supplemented with spatial distribution of melanin and HbO ₂ that indicated all skin tags were benign with no infiltration of vessels inside the melanin signal
[131]	Patients with pigmented skin lesions	HbO ₂ , HbR, and melanin	OCT, RCM, and PAI in combination enable image-guided bedside evaluation of suspicious pigmented skin tumors

Notes: PAI, photoacoustic imaging; PAM, photoacoustic microscopy; SC, stratum corneum; SB, stratum basale; CALM, café-au-lait macule; PA, photoacoustic; PWS, port-wine stains; PAMes, photoacoustic mesoscopy; FRSOM, fast RSOM; RSOM, raster-scan optoacoustic mesoscopy; UWB-RSOM, ultrawide spectrum and bandwidth RSOM; SWIR, short-wave infrared; PAT, photoacoustic tomography; 3D, three-dimensional; US, ultrasound; vMSOT, volumetric MSOT; MSOT, multi-spectral optoacoustic tomography; HbO₂, oxy-hemoglobin; HbR, deoxy-hemoglobin; OCT, optical coherence tomography; RCM, reflectance confocal microscopy.

are most apparent when looking at studies on target disease common to all three modalities. For instance, in PWS imaging studies, PAM had the advantage of imaging capillaries in a small FOV and can quantify the density and depth of blood vessels in lesions. Using the microstructural information, PAM can also provide quantitative diagnostic indices that are sensitive to alterations in the shallow skin layers. PAT can cover large skin areas that include almost an entire PWS lesion, whereas PAM can only analyze a small sample area of a lesion. PAT has poor spatial resolution and, therefore, cannot identify and analyze vascular geometry, but it can distinguish lesions by considering their relative signal intensities and indexing their severity.

While reviewing the recent literature, we found that most of the clinical skin PAI research was based on vascular imaging, and not many weights were put on the melanin analysis. PAI is able to visualize the non-superficial morphology and distribution of skin pigment, and we think it is worth investigating its clinical potential to provide a critical triaging modality for various pigmentation diseases such as melanoma or hypopigmentation disorders. To expand the range of application, more skin biomarkers having optical contrast (e.g., collagen and lipid) should be discovered with the use of multi-wavelength laser sources supporting up to the NIR-II range.

In terms of clinical application, niche positioning in the current clinical flow would be important. Generally speaking, many skin diagnoses are made from qualitative visual inspection often aided by optical techniques (e.g., Wood's lamp) or histologically analyzed by biopsy. In this aspect, PAI has great potential to fit between the two diagnostic methods, providing detailed visualization of non-superficial skin structures and quantitative analysis of the structural features. Still, the reliability and repeatability of PAI modalities should be validated in comparison to conventional techniques, and especially the effect of skin color on the PAI results should be investigated thoroughly. Due to the nature of optical and acoustic beams, the existence of thick scars, scabs, or calluses could also limit the application of PAI. Furthermore, PAI systems should be designed with extra care for hygiene because they require direct contact with the skin.

6. Conclusion

Overall, PAI technology can diagnose human skin non-invasively and potentially meet a variety of needs in dermatology such as staging, progression, and treatment monitoring. PAI also provides quantifiable metrics by analyzing the PA signal amplitudes that represent Hb or melanin contents observed in various scales using PAM, PAMes, or PAT. By adopting a fit-for-purpose PAI system, dermatologists will be able to effectively diagnose and test skin diseases, and reduce the number of repetitive treatments.

Acknowledgments

This work was supported by the National Research Foundation (NRF) (Nos. 2020R1A6A1A03047902, 2021M3C1C3097624, 2023R1A2C3004880, and RS-2024-00340633), the Korea Medical Device Development Fund (Nos. 1711195277 and RS-2020-KD000008), and the BK21 FOUR projects (POSTECH), funded by the Korean government (Ministry of Science and ICT, Ministry of Education, Ministry of Trade, Industry, and Energy, Ministry of Health and Welfare, and Ministry of Food and Drug Safety). Chulhong Kim has financial

interests in Opticho Inc., which, however, did not support this work.

References

1. A. G. Bell, "The photophone," *J. Franklin Inst.* **110**, 237 (1880).
2. Y. Fan *et al.*, "Development of a laser photothermoacoustic frequency-swept system for subsurface imaging: theory and experiment," *J. Acoust. Soc. Am.* **116**, 3523 (2004).
3. M. Xu and L. V. Wang, "Photoacoustic imaging in biomedicine," *Rev. Sci. Instrum.* **77**, 041101 (2006).
4. S. Takatani and M. D. Graham, "Theoretical analysis of diffuse reflectance from a two-layer tissue model," *IEEE Trans. Biomed. Eng.* **BME-26**, 656 (1979).
5. S. L. Jacques, R. D. Glickman, and J. A. Schwartz, "Internal absorption coefficient and threshold for pulsed laser disruption of melanosomes isolated from retinal pigment epithelium," *Proc. SPIE* **2681**, 468 (1996).
6. J. B. Dawson *et al.*, "A theoretical and experimental study of light absorption and scattering by *in vivo* skin," *Phys. Med. Biol.* **25**, 695 (1980).
7. S. H. Tseng *et al.*, "Chromophore concentrations, absorption and scattering properties of human skin *in-vivo*," *Opt. Express* **17**, 14599 (2009).
8. S. Choi *et al.*, "X-ray free-electron laser induced acoustic microscopy (XFELAM)," *Photoacoustics* **35**, 100587 (2024).
9. D. Kim *et al.*, "An ultraviolet-transparent ultrasound transducer enables high-resolution label-free photoacoustic histopathology," *Laser Photonics Rev.* **18**, 2300652 (2024).
10. J. Laufer *et al.*, "Quantitative spatially resolved measurement of tissue chromophore concentrations using photoacoustic spectroscopy: application to the measurement of blood oxygenation and haemoglobin concentration," *Phys. Med. Biol.* **52**, 141 (2007).
11. B. Park *et al.*, "Functional photoacoustic imaging: from nano- and micro- to macro-scale," *Nano Converg.* **10**, 29 (2023).
12. C. Cano *et al.*, "Deep learning assisted classification of spectral photoacoustic imaging of carotid plaques," *Photoacoustics* **33**, 100544 (2023).
13. C. Kim *et al.*, "In vivo molecular photoacoustic tomography of melanomas targeted by bioconjugated gold nanocages," *ACS Nano* **4**, 4559 (2010).
14. W. Choi *et al.*, "Recent advances in contrast-enhanced photoacoustic imaging: overcoming the physical and practical challenges," *Chem. Rev.* **123**, 7379 (2023).
15. B. Park *et al.*, "Listening to drug delivery and responses via photoacoustic imaging," *Adv. Drug Deliv. Rev.* **184**, 114235 (2022).
16. R. Gao *et al.*, "Background-suppressed tumor-targeted photoacoustic imaging using bacterial carriers," *Proc. Natl. Acad. Sci. U.S.A.* **119**, e2121982119 (2022).
17. R. Gao *et al.*, "Nonlinear mechanisms in photoacoustics—powerful tools in photoacoustic imaging," *Photoacoustics* **22**, 100243 (2021).
18. R. Gao *et al.*, "Breaking acoustic limit of optical focusing using photoacoustic-guided wavefront shaping," *Laser Photonics Rev.* **15**, 2000594 (2021).
19. Z. Huang *et al.*, "Multimodal PA/US imaging in rheumatoid arthritis: enhanced correlation with clinical scores," *Photoacoustics* **38**, 100615 (2024).
20. S. Wang *et al.*, "Tri-modality *in vivo* imaging for tumor detection with combined ultrasound, photoacoustic, and photoacoustic elastography," *Photoacoustics* **38**, 100630 (2024).
21. A. P. Träger *et al.*, "Hybrid ultrasound and single wavelength optoacoustic imaging reveals muscle degeneration in peripheral artery disease," *Photoacoustics* **35**, 100579 (2024).
22. Y. Yu *et al.*, "Simultaneous photoacoustic and ultrasound imaging: a review," *Ultrasonics* **139**, 107277 (2024).
23. X. Mu *et al.*, "On-demand expansion fluorescence and photoacoustic microscopy (ExFLPAM)," *Photoacoustics* **38**, 100610 (2024).
24. J. Park *et al.*, "Quadruple ultrasound, photoacoustic, optical coherence, and fluorescence fusion imaging with a transparent ultrasound transducer," *Proc. Natl. Acad. Sci. U.S.A.* **118**, e1920879118 (2021).
25. X. Wei *et al.*, "Deep learning-powered biomedical photoacoustic imaging," *Neurocomputing* **573**, 127207 (2024).
26. H. Zhao *et al.*, "Deep learning enables superior photoacoustic imaging at ultralow laser dosages," *Adv. Sci.* **8**, 2003097 (2021).
27. X. Zhu *et al.*, "Real-time whole-brain imaging of hemodynamics and oxygenation at micro-vessel resolution with ultrafast wide-field photoacoustic microscopy," *Light Sci. Appl.* **11**, 138 (2022).
28. X. Yang *et al.*, "Photoacoustic imaging for monitoring of stroke diseases: a review," *Photoacoustics* **23**, 100287 (2021).
29. R. Cao *et al.*, "Photoacoustic microscopy reveals the hemodynamic basis of sphingosine 1-phosphate-induced neuroprotection against ischemic stroke," *Theranostics* **8**, 6111 (2018).
30. Z. Chen *et al.*, "Multimodal noninvasive functional neurophotonic imaging of murine brain-wide sensory responses," *Adv. Sci.* **9**, 2105588 (2022).
31. V. Tsytisarev *et al.*, "Photoacoustic microscopy of microvascular responses to cortical electrical stimulation," *J. Biomed. Opt.* **16**, 1 (2011).
32. W. Liu *et al.*, "In vivo corneal neovascularization imaging by optical-resolution photoacoustic microscopy," *Photoacoustics* **2**, 81 (2014).
33. S. Hu *et al.*, "Label-free photoacoustic ophthalmic angiography," *Opt. Lett.* **35**, 1 (2010).
34. W. Liu and H. F. Zhang, "Photoacoustic imaging of the eye: a mini review," *Photoacoustics* **4**, 112 (2016).
35. S. Jiao *et al.*, "Photoacoustic ophthalmoscopy for *in vivo* retinal imaging," *Opt. Express* **18**, 3967 (2010).
36. D. Kim *et al.*, "In vivo quantitative photoacoustic monitoring of corticosteroid-induced vasoconstriction," *J. Biomed. Opt.* **28**, 082805 (2023).
37. A. B. E. Attia *et al.*, "A review of clinical photoacoustic imaging: current and future trends," *Photoacoustics* **16**, 100144 (2019).
38. E. Y. Park *et al.*, "Photoacoustic imaging systems based on clinical ultrasound platform," *Exp. Biol. Med.* **247**, 551 (2022).
39. H. Assi *et al.*, "A review of a strategic roadmapping exercise to advance clinical translation of photoacoustic imaging: from current barriers to future adoption," *Photoacoustics* **32**, 100539 (2023).
40. V. S. Dogra *et al.*, "Preliminary results of ex vivo multispectral photoacoustic imaging in the management of thyroid cancer," *AJR Am. J. Roentgenol.* **202**, W552 (2014).
41. A. Dima and V. Ntziachristos, "In-vivo handheld optoacoustic tomography of the human thyroid," *Photoacoustics* **4**, 65 (2016).
42. M. Yang *et al.*, "Photoacoustic/ultrasound dual imaging of human thyroid cancers: an initial clinical study," *Biomed. Opt. Express* **8**, 3449 (2017).
43. J. Kim *et al.*, "Multiparametric photoacoustic analysis of human thyroid cancers *in vivo*," *Cancer Res.* **81**, 4849 (2021).
44. B. Park, C. Kim, and J. Kim, "Recent advances in ultrasound and photoacoustic analysis for thyroid cancer diagnosis," *Adv. Phys. Res.* **2**, 2200070 (2023).
45. M. Toi *et al.*, "Visualization of tumor-related blood vessels in human breast by photoacoustic imaging system with a hemispherical detector array," *Sci. Rep.* **7**, 41970 (2017).
46. G. Diot *et al.*, "Multispectral optoacoustic tomography (MSOT) of human breast cancer," *Clin. Cancer Res.* **23**, 6912 (2017).
47. E. I. Neuschler *et al.*, "A pivotal study of optoacoustic imaging to diagnose benign and malignant breast masses: a new evaluation tool for radiologists," *Radiology* **287**, 398 (2018).
48. A. Karlas *et al.*, "Cardiovascular optoacoustics: from mice to men - a review," *Photoacoustics* **14**, 19 (2019).

49. M. Wu *et al.*, "Emerging technology update intravascular photoacoustic imaging of vulnerable atherosclerotic plaque," *Interv. Cardiol.* **11**, 120 (2016).
50. K. Jansen, G. van Soest, and A. F. W. van der Steen, "Intravascular photoacoustic imaging: a new tool for vulnerable plaque identification," *Ultrasound Med. Biol.* **40**, 1037 (2014).
51. H. Zafar *et al.*, "Photoacoustic cardiovascular imaging: a new technique for imaging of atherosclerosis and vulnerable plaque detection," *Biomed. Phys. Eng. Express* **4**, 032002 (2018).
52. W. Choi *et al.*, "Three-dimensional multistructural quantitative photoacoustic and US imaging of human feet in vivo," *Radiology* **303**, 467 (2022).
53. J. Yang *et al.*, "Detecting hemodynamic changes in the foot vessels of diabetic patients by photoacoustic tomography," *J. Biophotonics* **13**, e202000011 (2020).
54. S. Nemirova *et al.*, "Scanning optoacoustic angiography for assessing structural and functional alterations in superficial vasculature of patients with post-thrombotic syndrome: a pilot study," *Photoacoustics* **38**, 100616 (2024).
55. T. Chen *et al.*, "Dedicated photoacoustic imaging instrument for human periphery blood vessels: a new paradigm for understanding the vascular health," *IEEE Trans. Biomed. Eng.* **69**, 1093 (2022).
56. J. Ahn *et al.*, "High-resolution functional photoacoustic monitoring of vascular dynamics in human fingers," *Photoacoustics* **23**, 100282 (2021).
57. R. Huggenberger and M. Detmar, "The cutaneous vascular system in chronic skin inflammation," *J. Investig. Dermatol. Symp. Proc.* **15**, 24 (2011).
58. M. Lupu *et al.*, "Vascular patterns in basal cell carcinoma: dermoscopic, confocal and histopathological perspectives," *Oncol. Lett.* **17**, 4112 (2019).
59. H. R. Moreira and A. P. Marques, "Vascularization in skin wound healing: where do we stand and where do we go?" *Curr. Opin. Biotechnol.* **73**, 253 (2022).
60. P. Mabeta, "Paradigms of vascularization in melanoma: clinical significance and potential for therapeutic targeting," *Biomed. Pharmacother.* **127**, 110135 (2020).
61. S. Gupta *et al.*, "Dermal vasculature in psoriasis and psoriasiform dermatitis: a morphometric study," *Indian J. Dermatol.* **56**, 647 (2011).
62. R. Waelchli *et al.*, "New vascular classification of port-wine stains: improving prediction of Sturge-Weber risk," *Br. J. Dermatol.* **171**, 861 (2014).
63. M. Steinhoff *et al.*, "Role of vasculature in atopic dermatitis," *J. Allergy Clin. Immunol.* **118**, 190 (2006).
64. A. W. Barrett and A. D. Beynon, "A histochemical study on the distribution of melanin in human oral epithelium at six regional sites," *Arch. Oral Biol.* **36**, 771 (1991).
65. G. T. Pack, N. Lenson, and D. M. Gerber, "Regional distribution of moles and melanomas," *AMA Arch. Surg.* **65**, 862 (1952).
66. Y. Zhang *et al.*, "Chronic label-free volumetric photoacoustic microscopy of melanoma cells in three-dimensional porous scaffolds," *Biomaterials* **31**, 8651 (2010).
67. K. Abhishek and N. Khunger, "Complications of skin biopsy," *J. Cutan. Aesthet. Surg.* **8**, 239 (2015).
68. D. Oh *et al.*, "Contrast agent-free 3D renal ultrafast doppler imaging reveals vascular dysfunction in acute and diabetic kidney diseases," *Adv. Sci.* **10**, 2303966 (2023).
69. S. Cho *et al.*, "An ultrasensitive and broadband transparent ultrasound transducer for ultrasound and photoacoustic imaging in-vivo," *Nat. Commun.* **15**, 1444 (2024).
70. S. Jeon *et al.*, "A novel 2-D synthetic aperture focusing technique for acoustic-resolution photoacoustic microscopy," *IEEE Trans. Med. Imaging* **38**, 250 (2019).
71. H. Zhao *et al.*, "Motion correction in optical resolution photoacoustic microscopy," *IEEE Trans. Med. Imaging* **38**, 2139 (2019).
72. H. Zhao *et al.*, "Three-dimensional Hessian matrix-based quantitative vascular imaging of rat iris with optical-resolution photoacoustic microscopy in vivo," *J. Biomed Opt.* **23**, 1 (2018).
73. J. Meng *et al.*, "WSA-MP-Net: weak-signal-attention and multi-scale perception network for microvascular extraction in optical-resolution photoacoustic microscopy," *Photoacoustics* **37**, 100600 (2024).
74. C. Yoon *et al.*, "Deep learning-based virtual staining, segmentation, and classification in label-free photoacoustic histology of human specimens," *Light Sci. Appl.* **13**, 226 (2024).
75. H. Lee *et al.*, "Transportable multispectral optical-resolution photoacoustic microscopy using stimulated Raman scattering spectrum," *IEEE Trans. Instrum. Meas.* **73**, 4502309 (2024).
76. J. Ahn *et al.*, "In vivo photoacoustic monitoring of vasoconstriction induced by acute hyperglycemia," *Photoacoustics* **30**, 100485 (2023).
77. J. Chen *et al.*, "Wide-field polygon-scanning photoacoustic microscopy of oxygen saturation at 1-MHz A-line rate," *Photoacoustics* **20**, 100195 (2020).
78. R. Shintate *et al.*, "High-speed optical resolution photoacoustic microscopy with MEMS scanner using a novel and simple distortion correction method," *Sci. Rep.* **12**, 9221 (2022).
79. J. W. Baik *et al.*, "Super wide-field photoacoustic microscopy of animals and humans in vivo," *IEEE Trans. Med. Imaging* **39**, 975 (2020).
80. M. Zafar *et al.*, "Ultra-widefield and high-speed spiral laser scanning OR-PAM: system development and characterization," *J. Biophotonics* **16**, e202200383 (2023).
81. Z. Xie *et al.*, "Laser-scanning optical-resolution photoacoustic microscopy," *Opt. Lett.* **34**, 1771 (2009).
82. J. Kim *et al.*, "Deep learning acceleration of multiscale superresolution localization photoacoustic imaging," *Light Sci. Appl.* **11**, 131 (2022).
83. N. Chen *et al.*, "Video-rate high-resolution single-pixel non-scanning photoacoustic microscopy," *Biomed. Opt. Express* **13**, 3823 (2022).
84. U. A. T. Hofmann *et al.*, "Enhancing optoacoustic mesoscopy through calibration-based iterative reconstruction," *Photoacoustics* **28**, 100405 (2022).
85. J. Aguirre *et al.*, "Precision assessment of label-free psoriasis biomarkers with ultra-broadband optoacoustic mesoscopy," *Nat. Biomed. Eng.* **1**, 0068 (2017).
86. S. Cho *et al.*, "3D PHOVIS: 3D photoacoustic visualization studio," *Photoacoustics* **18**, 100168 (2020).
87. W. Kim *et al.*, "Wide-field three-dimensional photoacoustic/ultrasound scanner using a two-dimensional matrix transducer array," *Opt. Lett.* **48**, 343 (2023).
88. R. A. Kruger *et al.*, "Dedicated 3D photoacoustic breast imaging," *Med. Phys.* **40**, 113301 (2013).
89. J. Yang, S. Choi, and C. Kim, "Practical review on photoacoustic computed tomography using curved ultrasound array transducer," *Biomed. Eng. Lett.* **12**, 19 (2022).
90. C. Lee, C. Kim, and B. Park, "Review of three-dimensional handheld photoacoustic and ultrasound imaging systems and their applications," *Sensors* **23**, 8149 (2023).
91. C. Lee *et al.*, "Panoramic volumetric clinical handheld photoacoustic and ultrasound imaging," *Photoacoustics* **31**, 100512 (2023).
92. R. Gao *et al.*, "Restoring the imaging quality of circular transducer array-based PACT using synthetic aperture focusing technique integrated with 2nd-derivative-based back projection scheme," *Photoacoustics* **32**, 100537 (2023).
93. S. Choi *et al.*, "Deep learning enhances multiparametric dynamic volumetric photoacoustic computed tomography in vivo (DL-PACT)," *Adv. Sci.* **10**, 2202089 (2023).
94. S. Jeon *et al.*, "A deep learning-based model that reduces speed of sound aberrations for improved in vivo photoacoustic imaging," *IEEE Trans. Image Process.* **30**, 8773 (2021).

95. Z. Cheng *et al.*, "3D depth-coded photoacoustic microscopy with a large field of view for human skin imaging," *Chin. Opt. Lett.* **16**, 081701 (2018).
96. J. Ahn *et al.*, "Fully integrated photoacoustic microscopy and photoplethysmography of human in vivo," *Photoacoustics* **27**, 100374 (2022).
97. Z. Wang *et al.*, "Photoacoustic and ultrasound (PAUS) dermoscope with high sensitivity and penetration depth by using a bimorph transducer," *J. Biophotonics* **13**, e202000145 (2020).
98. Y. Gao *et al.*, "4D spectral-spatial computational photoacoustic dermoscopy," *Photoacoustics* **34**, 100572 (2023).
99. Z. Cheng *et al.*, "In vivo volumetric monitoring of revascularization of traumatized skin using extended depth-of-field photoacoustic microscopy," *Front. Optoelectron.* **13**, 307 (2020).
100. H. Ma *et al.*, "Quantitative and anatomical imaging of dermal angiopathy by noninvasive photoacoustic microscopic biopsy," *Biomed. Opt. Express* **12**, 6300 (2021).
101. B. Hindelang *et al.*, "Optoacoustic mesoscopy shows potential to increase accuracy of allergy patch testing," *Contact Dermatitis* **83**, 206 (2020).
102. B. Hindelang *et al.*, "Quantification of skin sensitivity to ultraviolet radiation using ultrawideband optoacoustic mesoscopy," *Br. J. Dermatol.* **184**, 352 (2021).
103. T. Nau *et al.*, "Raster-scanning optoacoustic mesoscopy biomarkers for atopic dermatitis skin lesions," *Photoacoustics* **31**, 100513 (2023).
104. Y. W. Yew *et al.*, "Investigation of morphological, vascular and biochemical changes in the skin of an atopic dermatitis (AD) patient in response to dupilumab using raster scanning optoacoustic mesoscopy (RSOM) and handheld confocal Raman spectroscopy (CRS)," *J. Dermatol. Sci.* **95**, 123 (2019).
105. X. Li *et al.*, "Multispectral raster-scanning optoacoustic mesoscopy differentiate lesional from non-lesional atopic dermatitis skin using structural and functional imaging markers," *Photoacoustics* **28**, 100399 (2022).
106. X. Li *et al.*, "Structural and functional imaging of psoriasis for severity assessment and quantitative monitoring of treatment response using high-resolution optoacoustic imaging," *Photoacoustics* **38**, 100611 (2024).
107. H. He *et al.*, "Opening a window to skin biomarkers for diabetes stage with optoacoustic mesoscopy," *Light Sci. Appl.* **12**, 231 (2023).
108. H. He *et al.*, "Fast optoacoustic mesoscopy of microvascular endothelial dysfunction in cardiovascular risk and disease," *bioRxiv* (2021).
109. C. P. Denton and D. Khanna, "Systemic sclerosis," *Lancet* **390**, 1685 (2017).
110. M. Masthoff *et al.*, "Multispectral optoacoustic tomography of systemic sclerosis," *J. Biophotonics* **11**, e201800155 (2018).
111. R. Rosenberry and M. D. Nelson, "Reactive hyperemia: a review of methods, mechanisms, and considerations," *Am. J. Physiol. Regul. Integr. Comp. Physiol.* **318**, R605 (2020).
112. L. Monteiro Rodrigues, T. F. Granja, and S. F. de Andrade, "Optoacoustic imaging offers new insights into in vivo human skin vascular physiology," *Life* **12**, 1628 (2022).
113. H. Zhang *et al.*, "Quantitatively assessing port-wine stains using a photoacoustic imaging method: a pilot study," *J. Am. Acad. Dermatol.* **85**, 1613 (2021).
114. H. Ma *et al.*, "Switchable optical and acoustic resolution photoacoustic dermoscope dedicated into in vivo biopsy-like of human skin," *Appl. Phys. Lett.* **116**, 073703 (2020).
115. H. Ma *et al.*, "Three dimensional confocal photoacoustic dermoscopy with an autofocusing sono-opto probe," *J. Biophotonics* **15**, e202100323 (2022).
116. H. Ma *et al.*, "Fast linear confocal scanning photoacoustic dermoscopy for non-invasive assessment of chromatodermatosis," *Appl. Phys. Lett.* **113**, 083704 (2018).
117. H. Ma *et al.*, "Multiscale confocal photoacoustic dermoscopy to evaluate skin health," *Quantum Imaging Med. Surg.* **12**, 2696 (2022).
118. Z. Wang *et al.*, "Bifocal 532/1064 nm alternately illuminated photoacoustic microscopy for capturing deep vascular morphology in human skin," *J. Eur. Acad. Dermatol. Venereol.* **36**, 51 (2022).
119. Z. Wang *et al.*, "Quantitative classification of melasma with photoacoustic microscopy: a pilot study," *J. Biomed. Opt.* **29**, S11504 (2024).
120. H. He *et al.*, "Fast raster-scan optoacoustic mesoscopy enables assessment of human melanoma microvasculature in vivo," *Nat. Commun.* **13**, 2803 (2022).
121. A. Berezhnoi *et al.*, "Optical features of human skin revealed by optoacoustic mesoscopy in the visible and short-wave infrared regions," *Opt. Lett.* **44**, 4119 (2019).
122. A. Breathnach *et al.*, "Preoperative measurement of cutaneous melanoma and nevi thickness with photoacoustic imaging," *J. Med. Imaging* **5**, 1 (2018).
123. M. Crisan *et al.*, "Ultrasonographic staging of cutaneous malignant tumors: an ultrasonographic depth index," *Arch. Dermatol. Res.* **305**, 305 (2013).
124. J. Kim *et al.*, "Multispectral ex vivo photoacoustic imaging of cutaneous melanoma for better selection of the excision margin," *Br. J. Dermatol.* **179**, 780 (2018).
125. B. Park *et al.*, "3D wide-field multispectral photoacoustic imaging of human melanomas in vivo: a pilot study," *J. Eur. Acad. Dermatol. Venereol.* **35**, 669 (2021).
126. A. F. Kukk *et al.*, "Combined ultrasound and photoacoustic C-mode imaging system for skin lesion assessment," *Sci. Rep.* **13**, 17947 (2023).
127. A. F. Kukk *et al.*, "Non-invasive 3D imaging of human melanocytic lesions by combined ultrasound and photoacoustic tomography: a pilot study," *Sci. Rep.* **14**, 2768 (2024).
128. A. E. Attia *et al.*, "Non-invasive photoacoustic 3D imaging of non-melanoma skin cancers in Asian population," in *Biophotonics Congress: Biomedical Optics Congress 2018 (Microscopy/Translational/Brain/OTS)* (2018), paper CF3B.7.
129. S. Y. Chuah *et al.*, "Volumetric multispectral optoacoustic tomography for 3-dimensional reconstruction of skin tumors: a further evaluation with histopathologic correlation," *J. Invest. Dermatol.* **139**, 481 (2019).
130. G. Fredman *et al.*, "Skin tags imaged by reflectance confocal microscopy, optical coherence tomography and multispectral optoacoustic tomography at the bedside," *Skin Res. Technol.* **27**, 324 (2021).
131. T. Von Knorring *et al.*, "Differentiation between benign and malignant pigmented skin tumours using bedside diagnostic imaging technologies: a pilot study," *Acta Derm. Venereol.* **102**, adv00634 (2022).
132. J. Yao and L. V. Wang, "Sensitivity of photoacoustic microscopy," *Photoacoustics* **2**, 87 (2014).
133. W. Xia *et al.*, "Handheld real-time LED-based photoacoustic and ultrasound imaging system for accurate visualization of clinical metal needles and superficial vasculature to guide minimally invasive procedures," *Sensors* **18**, 1394 (2018).